## *Structural evolution during cyclic glacier surges 1*

Hambrey, Michael; Clarke, Garry K. C.

*Published in:*
Journal of Geophysical Research: Earth Surface

*DOI:*
10.1029/2018JF004869

*Publication date:*
2019

*Citation for published version (APA):*
Hambrey, M., & Clarke, G. K. C. (2019). Structural evolution during cyclic glacier surges 1: Structural glaciology of Trapridge Glacier, Yukon, Canada. *Journal of Geophysical Research: Earth Surface*, *124*(2), 464-494. https://doi.org/10.1029/2018JF004869

# Structural evolution during cyclic glacier surges: 1. Structural glaciology of Trapridge Glacier, Yukon, Canada

Michael J. Hambrey[1] and Garry K. C. Clarke[2]

Garry Clarke, clarke@eoas.ubc.ca

[1]Centre for Glaciology, Department of Geography and Earth Sciences, Aberystwyth University, Aberystwyth, Ceredigion, United Kingdom.

[2]Department of Earth, Ocean and Atmospheric Sciences, University of British Columbia, Vancouver, British Columbia, Canada.



This article has been accepted for publication and undergone full peer review but has not been through the copyediting, typesetting, pagination and proofreading process, which may lead to differences between this version and the Version of Record. Please cite this article as doi: 10.1029/2018JF004869

**Abstract.** Interpreting the relationships among the internal processes of glaciers and their mesoscale structural products has been a longstanding challenge for glaciologists. Trapridge Glacier is a small polythermal surge-type valley glacier that has been studied for 40 years. It offers an opportunity to investigate the structural evolution of a glacier through a series of surges, and to apply novel modeling approaches to gain physical insight as to how different structures are formed. Following the glacier's most recent slow surge, the structural attributes were documented, with emphasis on their three-dimensional geometry and sequential development: ice stratification ($S_0$), longitudinal foliation ($S_1$) and associated medial moraine, folding of stratification ($F_1$), transverse foliation ($S_2$), thrusts ($S_3$) and recumbent folds ($F_3$), fractures (surface crevassing and crevasse traces) ($S_4$). Efforts to represent these structures using models of glacier flow dynamics remain at an early stage but provide informative tests of model skill and of current understanding of the processes that control structure generation. Using field interpretations as a guide to the relevant processes of formation, structures on Trapridge Glacier are compared with computer-simulated structures for the same glacier. Modeling achieved the greatest success in simulating moraine patterns, ice stratification, longitudinal foliation, and the downglacier decrease in the density of surface crevasse traces. The least successful effort was to simulate the orientation of crevasse traces.

**Keypoints:**

- The formation and evolution of structures in a polythermal surging glacier have been subjected to combined field and modeling analysis.
- The model-calculated deformation gradient reveals how total strain influences the development of longitudinal foliation in glaciers.
- Crack modeling yields an explanation for the observed downglacier decrease in fracture density at the glacier surface.

## 1. Introduction

The aim of this paper is to describe, evaluate, and model the structures of a polythermal glacier as it progressed through a slow surge ca. 1980–2000 [*Frappé-Sénéclauze & Clarke*, 2007]. Slow surging is a little-studied phenomenon that shows many of the attributes of a conventional surge but is less intense and lasts far longer. A focus of the field study was on discriminating between structures formed during quiescence and those developed as a surge front moved through the glacier. An important function of the modeling effort is to test whether the surging and non-surging variants of the same model were equally effective at generating the observed structures. In a companion paper [*Clarke & Hambrey*, 2019] we present details of the physics and numerics of the model and use idealized diagnostic models to explore a range of influences on structure generation.

Several studies have been undertaken on the structural evolution of surge-type glaciers. The most detailed has been on the temperate Variegated Glacier in SE Alaska, following the 1982–1983 surge, where foliation-development characterized quiescent-phase deformation, and crevasse formation and thrusting characterized surge-phase deformation [*Lawson*, 1994]. Polythermal glaciers in Svalbard, where the surge phase typically lasts several years, have also received attention [*Dowdeswell & Lindsay Collin*, 1990; *Hambrey et al.*, 1996; *Glasser et al.*, 1998; *Murray et al.*, 2000; *Murray & Booth*, 2010; *Woodward et al.*, 2002; *King et al.*, 2015; *Sevestre et al.*, 2018]. These studies explored the relationships among foliation, crevasses, crevasse traces, and thrusts in both their quiescent and active states.

Trapridge Glacier is well-suited to investigations of structural evolution. For four decades this glacier has been studied from perspectives that include thermal regime [*Jarvis & Clarke*, 1975; *Clarke & Blake*, 1991; *Frappé-Sénéclauze & Clarke*, 2007], glacier hydrology [*Stone & Clarke*, 1993; *Murray & Clarke*, 1995; *Clarke*, 1996; *Stone et al.*, 1997; *Flowers & Clarke*, 2000, 2002a, b], and basal flow and subglacial till deformation [*Blake et al.*, 1992; *Fischer & Clarke*, 1997a, b; *Fischer et al.*, 1999]. Until now, however, the structure of the glacier has not been evaluated. In 2006, the development of ice-marginal cliff sections enabled a unique three-dimensional perspective to be obtained.

This contribution focuses on the formation and transport of medial moraines, the development of stratification and foliation structures, fold and thrust structures exposed in the terminal cliff, and characteristics of crevasse traces at the glacier surface. We also focus on a number of elevated surfaces on the glacier ("mounds") which are inferred to be related to uneven bed topography and hence to potential "sticky spots". Differences between the structural assemblages associated with the slow surge and those found on faster surge-type glaciers and differences between structures in surging and non-surging glaciers are of special interest. Structural development in glaciers, whether surging or not, appears to be highly individual, and thus field comparisons can be misleading. Comparative modeling offers a new approach.

Structural investigations have wide-ranging implications regarding the dynamic history of glaciers. This is especially true today when most glaciers are receding and downwasting, and where structures reveal a more dynamic state in the past (*Hambrey et al.*, 2005; *Lovell et al.*, 2015a). Numerical modeling allows past dynamic history to be quantified in terms of stress and cumulative strain, and provides a better understanding of

physical processes. Such approaches have been applied to ice caps and valley glaciers with steady-state flow characteristics (*Hudleston & Hooke*, 1980; *Hubbard & Hubbard*, 2000; *Hambrey et al.*, 2005), but this paper represents a first attempt to model structural evolution in a surge-type glacier.

## 2. Topographic and Glaciological Context of Trapridge Glacier

Trapridge Glacier is a ∼4 km-long outlet glacier on the eastern flanks of Mt. Wood (61°14′N, 140°20′W) in Kluane Park Reserve, Yukon, Canada (Figure 1). The glacier has two main flow units (south and north) separated by a prominent medial moraine, and there is also a dynamically separate and slow-moving "northern arm" which forms a broad unconstrained moraine. Trapridge Glacier surged prominently in the 1940s, and relict crevasses from the surge are clearly visible in 1951 aerial photographs. Following this event, the glacier stagnated in situ until a new surge front, evident in 1970s aerial photographs, began to move through the glacier. By the early 21st century much of the lower glacier had melted, leaving behind a sheet of basal till. Meanwhile, the surge front reached the apparent snout and was overriding the basal till zone. Field examination of glacier structure occurred in July–August 2006 (year 2006.6 in decimal years). Conditions at that time were not particularly favorable for surface structural investigation because of the short duration that the tongue was snow-free. Furthermore, there are no high-resolution photographic or satellite images available for mapping glacier-wide structures. Hence detailed structural mapping was not feasible, although the geometrical characteristics of key structures were documented.

According to the geophysical classification (*Ahlmann*, 1935), Trapridge Glacier is sub-polar. Its mean annual surface temperature is sub-freezing whereas a large part of the

glacier bed is at the melting point (*Jarvis & Clarke*, 1975; *Clarke & Blake*, 1991). Thus the glacier is polythermal but, unlike the idealized thermal structures proposed in *Blatter & Hutter* (1991), there is no evidence for a temperate ice layer of finite thickness. During the slow surge, temperatures of $-7°C$ were measured at 15 m depth at an experimental site in the lower tongue. Here the ice was 60–70 m thick and the velocity rose from $14\,m\,a^{-1}$ in 1974 to $42\,m\,a^{-1}$ in 1984, dropping to $9\,m\,a^{-1}$ in 2005 after passage of the surge front [*Frappé-Sénéclauze & Clarke*, 2007]. Basal conditions are well known in the warm-based middle part of the glacier, which was surrounded by a perimeter of cold-based ice [*Clarke et al.*, 1984; *Blake et al.*, 1992]. A bed of permeable till was identified, which was deforming to a depth of at least 0.3 m [*Blake et al.*, 1992]. Sliding and bed deformation accounted for up to 90% of the velocity in the late 1990s where the basal ice was demonstrably at the pressure melting point [*Flowers & Clarke*, 2002b].

## 3. Structural Evolution Through a Surge Cycle

Trapridge Glacier is known to have surged previously in the 1940s. A photograph by R. P. Sharp from 1941 [*Frappé-Sénéclauze & Clarke*, 2007, Fig. 1] shows a surge front in roughly the same position as the marginal cliff of the latest surge, advancing into an area of seemingly stagnant ice. Spanning the period from 1951 to 1981, a series of Canadian Government aerial photographs (Figure 2) shows the termination of the 1940s surge and the development of the most recent surge.

Ice extent in 1951 (Figure 2a) shows that the glacier tongue was almost entirely crevassed and close to its maximum position. Crevasses, which were mainly transverse and diagonal in orientation, were heavily ablated and many were water-filled. The surge shows a subsidiary lobe at the northern margin, apparently related to a longitudinal debris mound

that diverted part of the flow away from the main trunk. The same mound was visible in 2006, when it was noted to be ice-cored. Ice in this mound thus predates the 1940s surge. *Frappé-Sénéclauze & Clarke* [2007] noted that the 1940s surge lasted no more than a decade, quite different from the slow-build-up of the recent surge. The intensity of crevassing suggests that the 1940s surge was a typical surge rather than a slow one.

The 1972 ice extent (Figure 2b) shows that all crevasses in the lower glacier, apparent in Figure 2a, had by now ablated, revealing a medial moraine, strong longitudinal foliation, and supraglacial streams. The northern margin was covered by extensive debris, and a diagonal debris-draped limestone ridge projected through the ice. In contrast, the middle part of the glacier was reactivated as a new surge front moved through the glacier. This was denoted by a prominent bulge, truncating the medial moraine, behind which were extensive areas of transverse, diagonal and longitudinal crevasses, as well as extensive crevasse-free areas.

In 1977 (Figure 2c) the dead ice area was still prominent with its longitudinal foliation, supraglacial stream network, and bedrock ridge. Debris cover (known to be basal from 2006 observations) was more extensive than in 1972. The surge front was more prominent with crevasses of variable orientation, but the glacier surface still had extensive areas of crevasse-free ice. The medial moraine was visible in the surge front for a short distance upglacier. By 1981 (Figure 2d), the dead ice area showed less exposed ice and more extensive areas of basal debris. The surge front and active glacier ice behind was similar to that in 1977. For subsequent years, no equivalent aerial photographs are available for comparison, but by 2006 ground observations showed that the original dead ice area was

no longer visible, although remnants were suspected under a cover of till. The surge front formed a terminal cliff that was slowly back-wasting.

## 4. Post-surge Structural Attributes

Structural observations from the surge phase itself are limited, but, following complete cessation of the surge in 2005 [*Frappé-Sénéclauze & Clarke*, 2007], the ice surface became more accessible, and most of the lower glacier tongue could be investigated. By this time, the surge front coincided with the visible terminus of the glacier, having advanced several hundred meters further than in 1981, when the last aerial photograph was taken. Structures are described in the order in which they evolved in the glacier as determined from cross-cutting relations, and using standard structural geological notation for planar structures and folds (Table 1).

### 4.1. Overall Structure and Medial Moraine Pattern

Trapridge Glacier is a composite glacier, with two main flow units (north and south), separated by a medial moraine (Figure 3). Field measurements indicate that each flow unit has a slightly different structural history. The medial moraine defines the average flow direction close to the centerline. Where excavated, the moraine forms a 5–10 cm cover of debris over apparently clean ice. Debris comprises mainly angular cobbles and lesser proportions of pebbles and boulders. Sand and granules from this moraine are concentrated in places by supraglacial streams. The debris is angular and interpreted as being of supraglacial origin, and the source of the debris is clearly associated with a steep unstable rock face that forms the glacier headwall. In contrast to the main tongue, a dynamically separate extension of the north flow unit, which appears not to have been

involved in the most recent surge, displays prominent regular layering. This is interpreted as primary stratification, which comprises low-dip layers that individually can be followed for more than 100 m; in one place an unconformity was observed. Few fractures are visible in this part of the glacier.

In the following sections we describe the observed 2006.6 stratification and foliation structures (Figures 4 and 5), fold structures (Figure 6), and fractures and crevasse traces (Figure 7). We then develop models of the formation and evolution of these structures and compare simulation results with field observations.

### 4.2. Stratification ($S_0$) and Folding ($F_1$)

The first structure to appear in the glacier below the temporary snow-line, labeled $S_0$, was a set of continuous gently dipping layers of coarse bubbly ice separated by diffuse dirty bubbly layers. This structure is especially visible in the higher part of the ablation area (Figure 4a), but is not well preserved in the lower glacier tongue. Its association with snowpack-layering indicates that the structure is primary stratification. It displays an open wavy style of folding ($F_1$), and locally a tighter similar-style of folding, associated with which is a weak axial-planar foliation ($S_1$). Fold axes, where measured, have a low upglacier plunge. Locally, stratification is associated with debris of supraglacial character (angular clasts; few fines).

### 4.3. Longitudinal Foliation ($S_1$)

Longitudinal foliation is ubiquitous throughout the tongue of Trapridge Glacier, but is commonly faint (Figure 4b). It is best developed close to the medial moraine, to which it is parallel. For this near-vertical structure, foliation is defined principally by crystal size,

bubble elongation, and bubble density, variations of which ablate at different rates giving a ridge-and-furrow appearance. The foliation is commonly rotated, or offset between fractures (described as crevasse traces). Locally, especially near the northern margin, foliation is parallel to mud layers (including orange clay). The geometry of longitudinal foliation is less consistent than in most valley glaciers. Nevertheless, on plotting three-dimensional data of poles to foliation across the lower glacier tongue, there is strong clustering (Figure 5) on stereonets.

Points on the scatterplot of Figure 5 correspond to the stereographic projection of points onto the surface of the lower hemisphere of a unit sphere. Each point $p$ is associated with the intersection of a unit vector $n_j^{\mathrm{p}} = [n_1^{\mathrm{p}}, n_2^{\mathrm{p}}, n_3^{\mathrm{p}}]$ with the surface of the this hemisphere. Given $N$ data points and sufficiently large $N$, the structure tensor is $\Upsilon_{jk} = \langle n_j^{\mathrm{p}} n_k^{\mathrm{p}} \rangle$, where angular brackets indicate averaging over the $N$ data points, e.g., $\langle n_1^{\mathrm{p}} n_2^{\mathrm{p}} \rangle = \frac{1}{N} \Sigma_{p=1}^{N} n_1^{\mathrm{p}} n_2^{\mathrm{p}}$. The tensor is symmetric and its eigenvalues and eigenvectors are readily calculated (Table 2). The $\mathbf{N}_1$ eigenvector, which is associated with the largest eigenvalue $\lambda_1$, is sub-horizontal and has north–south alignment, indicating that the dip of the plane of the foliation is near-vertical and the strike direction is east–west, roughly aligned with the ice flow direction. Foliation is commonly associated with sub-meter-scale folds but, despite a search, only a handful of these were observed at Trapridge Glacier. Where measured, the fold axes deviated somewhat from parallelism with flow.

From field observations, the foliation is interpreted as having formed in a simple shear regime, where wide flow units converge to form a narrower tongue, a feature of many polythermal glaciers with multiple accumulation basins, e.g., White Glacier on Axel Heiberg Island [*Hambrey & Müller*, 1978] and Midtre Lovénbreen in Svalbard [*Hambrey et al.*,

2005]. The distortion of foliation in places is inferred to be the result of rotation of inter-crevasse blocks, deflection by subglacial ridges or the result of sticky spots (e.g., locally frozen areas) at the bed.

### 4.4. Transverse Foliation ($S_2$)

Confined to the south flow unit, this structure consists of poorly defined anastomosing layers of coarse clear ice within a predominantly coarse bubbly ice mass. Where observed in mid-tongue this foliation dipped at 30–50° upglacier, but probably started with near-vertical dip. This structure is interpreted as originally forming as crevasse traces in a zone of transverse crevassing, followed by longitudinal compression. Similar structures, albeit much more pronounced, have been recorded below icefalls in Blue Glacier, Washington [*Allen et al.*, 1960], and Griesgletscher, Swiss Alps [*Hambrey and Milnes*, 1977].

### 4.5. Low-angle Fractures, Associated Debris ($S_3$), and Recumbent Folding ($F_3$)

The terminal cliff of Trapridge Glacier displays a series of prominent coarse-clear ice and debris layers, commonly extending for tens of meters where clean washed surfaces were available, spaced typically up to a meter. These structures intersect the longitudinal foliation, which shows up weakly in the cliff. These ice and debris layers are intimately associated with meter-scale recumbent folding of both similar and isoclinal types, with decimeter-scale parasitic folds being common on the limbs of the larger folds (Figure 6a). Fold axes appeared to be near-horizontal and subparallel to the ice front. The debris layers are themselves folded; alternatively, they bound complex folded zones (Figure 6b). Most of these layers dip downglacier, but less steeply than the underlying bed, so they tend to converge towards the bed and, in the other direction, some terminate abruptly

(Figure 6c). The debris that melts from these layers is poorly sorted, ranging in size from silt to boulder, which can be classed as muddy boulder-gravel or clast-rich muddy diamicton. Clasts shapes are predominantly subangular and subrounded, and some clasts are striated. The structures closely resemble those described in surge-type Tunabreen in Svalbard (*Lovell et al.*, 2015b).

These low-angle fractures are interpreted as thrusts on account of their asymptotic relationship with the bed and with each other, while the debris has the texture and clast-shape characteristics of basal debris that has been elevated to a higher position. Thrusts have been described from other polythermal glaciers that surge, notably in Svalbard including Kongsvegen [*Glasser et al.*, 1998; *Murray & Booth*, 2010], and Bakaninbreen [*Hambrey et al.*, 1996; *Murray et al.*, 2000]. However, all these thrusts are geometrically different, notably in being higher angle (typically with an upglacier dip of up to 50°). The recumbent folding is believed to be synchronous with an on-going thrusting process, because both the debris layers are themselves folded, and the folds themselves have sheared off lower limbs. The all-pervasive nature of this process along the terminal cliff suggests that propagation of the surge front is accomplished by deformation of the glacier bed [*Clarke & Blake*, 1991], which is manifested in terms of thrusting and folding of debris layers.

### 4.6. High-angle Fractures and Veins ($S_4$)

A variety of high-angle fractures and veins, referred to as crevasse traces, are the most noticeable structures on the surface of Trapridge Glacier. They are all-pervasive and are of many different orientations; their geometry and orientation are considered in the following section. Fracture sets are commonly parallel to the relatively small number of surviving open crevasses. These include sharply defined narrow transverse crevasses

(50 cm wide) in the higher part of the ablation area to broad open ablated longitudinal crevasses near the snout (Figure 7a). Fractures range in length from a few meters (Figure 7b) to 10s of meters. They commonly intersect each other, as well as the foliation (Figure 7c), sometimes displaying displacements of a few centimeters. Fractures are of two types: water-frozen fractures from a few centimeters to over a meter wide comprising candle-like ice crystals; thin cracks on the glacier surface which on close inspection are veins a few centimeters wide, comprising clear ice crystals extending orthogonally from coarse bubbly ice sides, and with a central suture. These attributes are observable only when weathered ice is removed (Figure 7d). The presence of so many crevasse traces influences supraglacial drainage, and many examples of streams flowing along the fractures, including changing direction where intersections occurred, were observed.

### 4.7. Fracture Analysis

The inferred crevasse traces ($S_4$) were systematically measured in the field in two- and three-dimensions to establish how their geometry and density changed along the flow-centerline of the glacier, and the significance of glacier surface-mounds in relation to subglacial topography. Sampling sites are illustrated in Figure 1c.

#### 4.7.1. Fracture Orientation

Poles to crevasse traces are plotted on lower hemisphere equal-area (Schmidt) projections from six sites along the flow-centerline (Figure 1c), broadly defined by the medial moraine and surveyed flow marker stakes, and from three glacier surface-mounds (Figure 1c), including one (FC3) which represents both sets of data. Data are presented as scatter-plots, contour-plots, and two-dimensional rose diagrams (Figure 8).

On the flow-centerline three-dimensional plots show a range of cluster styles and variable relationships with flow direction (Figure 8). Clusters are tight, broad girdles or double-peaked, with one girdle (FC1) showing that the majority of crevasse traces are parallel to flow. In contrast FC2 shows crevasse traces aligned orthogonal to flow. The other sites (FC3–FC5, FC7) show no systematic relationship to flow direction. Where present, open crevasses tend to be parallel to the dominant grouping of crevasse traces.

Two of the surface mounds (M1, M4) have two crevasse-trace maxima, orthogonal to each other, one of which coincides with the trend of open crevasses, but the relationship with flow direction is only clear in one case (45° to both maxima) (Figure 8). A third mound (M3 not plotted) has one strong and one weak maximum, with flow direction slightly offset from the first.

#### 4.7.2. Fracture Density

Overall, fracture density varied from 0.64 to 3.02 $\mathrm{m}^{-2}$ (obtained from Figures 9 and 10 by dividing the counts by the 50 $\mathrm{m}^2$ sampled area). Along the flow-centerline the crack density is variable, with a peak near the middle basin and a decline towards the snout. Density values for the glacier surface-mounds (M1–M3, FC3) are inconsistent, but are higher than the average of 1.71 $\mathrm{m}^2$.

There is no consistent pattern of a particular class (transverse, diagonal, longitudinal) dominating, although, in all except one case, longitudinal fractures are least common. Summing all the available data (855 crevasse traces), the breakdown is: transverse 44%; diagonal 39%; and longitudinal 17%, suggesting that longitudinal extension (causing transverse fractures) was dominant following passage of the surge front.

## 5. Structure Modeling

A thermomechanical ice dynamics model for Trapridge Glacier is a necessary prerequisite to the structure modeling. For the surface topography of the ice dynamics model we used the Natural Resources Canada 30-meter Digital Elevation Model (DEM). Elevation data were converted from the native Yukon Albers projection to a Zone 7 UTM projection with the NAD27 geodetic datum, the same projection used for Trapridge Glacier field work dating from 1967 [*Collins*, 1972] to 2007. Ice masks for 1951, 1970, 1972, 1977, and 1981 were produced from georeferenced vertical aerial photography [*Frappé-Sénéclauze*, 2006] and the grid boundaries for the ice dynamics model were prescribed (green dashed outline in Figure 1b). Bed topography (Figure 11) for ice-covered regions within the computational grid was interpolated from a geophysically derived bed map [*Flowers & Clarke*, 1999] and, where measurements were lacking, estimated using a simplified version of the *Clarke et al.* [2013] method. Figure 11 also shows the modeled ice margin for 2006.6 (blue outline), the assumed equilibrium line altitude (ELA, green solid line), and the assumed maximum extent of the fast-sliding zone during surges (red outline with pink shading). The solid circles (red, black, and green) indicate three points at which rock debris is deposited on the glacier surface (these are associated with the steep headwall immediately to the west of these points). The centerline and mound sites (e.g., FC1 and M1) at which measured and modeled ice structures can be compared are also indicated. With the following exceptions the model parameters are identical to those in Table 1 of *Clarke & Hambrey* [2019]: $Z_{\mathrm{ela}}$=2550 m, $[\mathrm{d}\dot{b}/\mathrm{d}z]_{\mathrm{acc}}$=5.5556 $\times$ $10^{-3}\,\mathrm{yr}^{-1}$, $[\mathrm{d}\dot{b}/\mathrm{d}z]_{\mathrm{abl}}$=1.1111 $\times$ $10^{-3}\,\mathrm{yr}^{-1}$, $\mathcal{C}_{\mathrm{slide}}$=5.0 $\times$ $10^{-10}\,\mathrm{m\,yr}^{-1}\,\mathrm{Pa}^{-2}$, $\mathcal{C}_{\mathrm{surge}}$=5.0 $\times$ $10^{-9}\,\mathrm{m\,yr}^{-1}\,\mathrm{Pa}^{-2}$, $N_x$=186, $N_y$=96, $N_\xi$=31, and $N_\zeta$=11.

Thermomechanical ice dynamics models solve for ice thickness $H(x, y, t)$, temperature $T(x, y, z, t)$, and the velocity field $\mathbf{v}(x, y, z, t)$. Following *Greve & Blatter* [2009] we employ the shallow ice approximation. With the flow solution in hand, it is a short step to calculate the tensors for velocity gradient $L_{jk}$, deformation rate $D_{jk} = \frac{1}{2}(L_{jk} + L_{kj})$, spin $W_{jk} = \frac{1}{2}(L_{jk} - L_{kj})$, deviatoric stress $s_{jk}$, and other potentially useful quantities (for additional details see *Clarke & Hambrey* [2019]). We did this at every time $t_n$ and point $x_k$ in the $N_x \times N_y \times N_\xi$ computational grid and archived the results for a single 50-year cycle. The assumption of cyclic surging is helpful because it reduces the size of this archive without limiting the time span of the model. Non-surging versions of an otherwise identical model were obtained by setting $\mathcal{C}_{\text{surge}}$=$\mathcal{C}_{\text{slide}}$ to eliminate fast-flow episodes.

For the Trapridge Glacier model, surges are assumed to have 13-year duration, including a 3-year acceleration phase and a 2-year termination phase, followed by a 37-year quiescent phase. These assignments represent an effort to reconcile the general features of the most recent surge with an assumed 50-year cycle. In the model, surges are induced by expanding the area of an assumed fast-sliding zone (Figure 11) following *Clarke & Hambrey* [2019].

We examine how conditions for structure generation vary over a single surge cycle. We make a distinction between "kinematic structures", which are the passive consequence of glacier flow, and "dynamic structures", which are constructional and require work to be done. Examples of the former are moraine patterns, the $S_0$ stratification, and the $S_1$ foliation; examples of the latter are thrusting ($S_3$) and crevasse formation ($S_4$).

We associate dynamic structures with deformational work. Because ice is assumed to be incompressible in the glacier flow model, the modeled deformation of an ice parcel can involve changes of shape but not volume. Constrained by this limitation, the power

density of deformational work (rate of deformational work per unit volume ($\mathrm{W\,m^{-3}}$)) is $\mathcal{P}_\mathrm{D} = L_{jk}s_{jk} = D_{jk}s_{jk}$, where we assume the Einstein summation convention for repeated subscripts (hence $\mathcal{P}_\mathrm{D} = \Sigma_{j,k}L_{jk}s_{jk}$). For perspective, $\mathcal{P}_\mathrm{D}$ is proportional to the strain heating associated with internal friction of the ice flow (e.g., *Clarke et al.*, 1977) which is analogous to the heating that one experiences while repeatedly bending a paper clip. We assume that the rate of construction of dynamic structures is roughly proportional to $\mathcal{P}_\mathrm{D}$.

Figure 12 shows plots of time series for volume-averaged power density and for the rate of change of glacier area over one cycle of surging. From 1955–1985 (during the quiescent phase) power density varies slowly and monotonically as the glacier thickens; the rate of change of glacier area shifts from negative to positive around 1970, marking the change from post-surge disintegration to pre-surge buildup. (Fluctuations in this curve occur because ice area changes in discrete steps; thus time derivatives calculated by finite-differences have a saw-tooth character.) The maximum power density and maximum rate of change of ice area occur simultaneously around 1990 and then decrease from 1990–1998 when the surge terminates.

Comparing the time-averaged deformational power density (red dashed line) with that of a non-surging but otherwise identical model (green dashed line) shows only a small difference. In the same setting, surging and non-surging glaciers share the same task: to transfer solid precipitation from the accumulation area to the ablation area where ice is melted. They accomplish this in different ways: episodic transport of ice from one reservoir to another for surging and steady transport for non-surging. The slight difference between the time averages for these two extremes (Figure 12) suggests that one must be

cautious in assuming that surging glaciers are exceptionally vigorous geomorphic agents. They work fast but sporadically.

Figure 13 shows maps of vertically-integrated power density at various phases of the surge cycle. The surge onset is at 1985 and the snapshots for 1986, 1987, and 1988, indicated by yellow markers (Figure 12), show the accelerating phase of the surge; those for 1990 and 1995 show the fully-developed surge, and those for 2000 and 2005 the post-surge quiescence. The color scale is the same for all maps. Surge activation is first apparent in the map for 1986; from 1986–1988 the activation zone expands as it sweeps downglacier. To this point there is little change at the ice margins. By 1990 the activation zone has reached the terminus and the glacier front begins to advance down-valley. The power density plot (Figure 12) shows that the average rate of dissipation of deformational energy reaches a maximum at roughly the same time as the activation zone reaches the glacier terminus, at which time the rate of change of area increases dramatically. The surge terminates in 1998 and the maps for 2000 and 2005 show glacier-wide quiescence. Because of the assumption of a 50-year surge cycle, a map for 2035 would be identical to that for 1985.

### 5.1. Medial Moraine Pattern

The medial moraine is a prominent feature of Trapridge Glacier (Figure 3) and an obvious target for structure modeling. We trace, through time and space, the trajectories of surficial rock debris deposited in the glacier accumulation region at points near the headwall (solid red, black, and green circles in Figure 11). The debris tracks are englacial for the first segment and become supraglacial at emergence points in the ablation region. Because the flow is non-steady, the tracks and emergence points vary with time in a

complex manner. Details of the modeling approach are given in *Clarke & Hambrey* [2019]. Figure 14 compares the observed and modeled medial moraine tracks and glacier outline in July 2006 (2006.6). Differences between the observed and modeled pattern are expected and can be attributed to uncertainty in subglacial topography, to simplifications in the model (e.g., steady mass balance, prescribed fast-sliding zone, and periodic surge cycle), and to imprecise mapping of the medial moraine.

Figure 15 shows the modeled time-evolution of the glacier margin and medial moraine pattern as the glacier progresses through a single 50-year surge cycle. Model year 0 corresponds to the surge onset time as well to years 50, 100, etc. The ice outline for model year 0 (Figure 15a) resembles the 1981 aerial photograph (Figure 2d). The modeled post-surge extent (Figures 15a and 15b) is considerably less than that recorded in the 1951 aerial photograph (Figure 2a). The match between the observed and modeled post-surge states (Figures 2b and 15e) shows that after the vigorous 1940s surge the lower reaches of Trapridge Glacier retained large areas of stagnant ice for decades after the surge. By assuming periodic surging and a steady mass balance, the model ignores the substantial effects of climate change in the study region. When the sliding parameters $\mathcal{C}_{\text{slide}}$ and $\mathcal{C}_{\text{surge}}$ were assigned, the aim was to approximate the recent slow surge rather than the 1940s fast surge. Thus the modeled maximum ice limits agree well with the slow surge limits and greatly underestimate the 1940s maximum limits suggested in Figure 2a.

### 5.2. Stratification $S_0$

Primary sedimentary stratification, $S_0$ (Figure 4a) is a structure found in the upper reaches of many valley glaciers (*Hambrey*, 1975; *Goodsell et al.*, 2005; *Hambrey et al.*, 2005; *Jennings et al.*, 2014, 2015), but flow convergence, complex flow over icefalls, and

surging can erase the record of this structure. On Trapridge Glacier, $S_0$ is clearly displayed in layered firn (Figure 4a), but is barely discernible in exposed glacier ice, except in its northern arm. For Trapridge Glacier, the surfaces of $S_0$ are interpreted as isochronal and this is the key assumption of our effort to model them.

Adapting earlier work on tracer transport modeling [*Clarke & Marshall*, 2002; *Clarke et al.*, 2005; *Lhomme et al.*, 2005], we use a semi-Lagrangian method to track the depositional age $t_d$ of all points in the computational grid. Figure 16 shows contours of the modeled depositional date of the exposed ice surface at 2006.6. In nature, the visual record of annual depositional surfaces is less regular than that of Figure 16 and distinguished by varying concentrations of dust and fine-grained debris.

Qualitatively the results are akin to the $S_0$ map for the Norwegian glacier, Charles Rabots Bre [*Hambrey*, 1975, Fig. 2] but we have no observational basis for evaluating the simulated $S_0$ stratification of Trapridge Glacier. Nonetheless, Figure 16 contains temporal information that has potential value for guiding field interpretations. Excluding the near-vertical terminal ice cliff for which surface ages are not plotted, the oldest exposed surface ice is ca. 1800 and for most of the exposed ice the age range is 1850–1950. Table 3 gives the modeled age of ice at the measurement sites. As examples, the model calculates that surface ice at FC1 was deposited in 1986.4 whereas surface ice at FC7 was deposited in 1836.2. Thus, according to the model, ice at FC1 has experienced a single surge while ice at FC7 has experienced four cycles of surging. After four surges it is not surprising that there is no observable trace of the $S_0$ stratification at FC7.

### 5.3. Longitudinal Foliation $S_1$

Longitudinal foliation ($S_1$) has been described from several valley glaciers (e.g., *Allen et al.*, 1960; *Hambrey & Müller*, 1978; *Hambrey et al.*, 2005; *Jennings et al.*, 2014). On Trapridge Glacier, $S_1$ is characterized by a longitudinal orientation and high dip angles as indicated in the stereographic projections (Figure 5) which are replicated here as Figure 17a. The foliation is thought to be associated with large total strains which cause strain ellipsoids to become flattened and disk-like; the foliation plane is perpendicular to the direction of maximum shortening (*Hooke & Hudleston*, 1978).

From a modeling perspective the $S_1$ foliation is best approached by calculating strain ellipsoids and, from these, inferring the orientation of their axes. A direct approach to calculating geometric parameters of the strain ellipsoid is to evaluate the deformation gradient tensor $F_{jk}$ [e.g., *Clarke & Hambrey*, 2019] from which the cumulative rotation, ellipsoid geometry, and other strain indicators can be obtained. The orientation of the minor axis of the strain ellipsoid is particularly relevant to the $S_1$ foliation because this indicates the direction of flattening. We therefore test the hypothesis that there is close correspondence between the plane of flattening and the plane of foliation.

For additional insight it is useful to refer to some specific examples. Table 3 summarizes the geometric parameters $\lambda_k^{\mathbf{V}}$ and $\mathbf{N}_k^{\mathbf{V}}$ of simulated strain ellipsoids calculated from the Trapridge Glacier model at the flowline and mound measurement sites. Additional information such as the ice deposition date, axis ratios, and dip angle of the foliation plane are also tabulated. In Table 3 the magnitude of the $z$ component of $\mathbf{N}_3^{\mathbf{V}}$ indicates whether the axis of maximum shortening is near-horizontal ($[N_3^{\mathbf{V}}]_z \rightarrow 0$, hence a steeply-dipping plane) or near-vertical ($[N_3^{\mathbf{V}}]_z \rightarrow 1$, hence a near-horizontal plane). The axis ratio $\kappa_{1:2}=\lambda_1^{\mathbf{V}}/\lambda_2^{\mathrm{V}}$

indicates whether the major and intermediate axes of the strain ellipsoid resemble a circle ($\kappa_{1:2} \approx 1$) or an elongated ellipse $\kappa_{1:2} \gg 1$; the axis ratio $\kappa_{2:3}$ indicates the degree of flattening. Factors that might favor development of the $S_1$ foliation are large values of the dip of the foliation plane ($\delta_3 > 30°$) and substantial ellipsoid flattening ($\kappa_{2:3} > 5$). Sites having ellipsoid geometries that are most favorable for foliation ($\kappa_{2:3} > 5$) are FC3, FC4, FC5, M3, and M4; those that are least favorable ($\kappa_{2:3} < 2$) are FC1, FC7, M1, and M2.

Figure 17a indicates that points on the scatterplot correspond to poles of the $\mathbf{N}_3^{\mathbf{V}}$ unit vector, though we have no measurements of the strain ellipsoid at these sites. Following this logic, the simulated deformation gradient at 121 surface sites for the modeled glacier can be used to evaluate strain ellipsoid parameters, as for Table 3, and plot poles of $\mathbf{N}_3^{\mathbf{V}}$ for each site (Figure 17b). At this stage the observed and modeled results are not directly comparable. We have plotted all the modeled points, irrespective of whether they favor foliation development. In contrast, all the points that correspond to actual field observations were presumably selected because they were associated with a discernible $S_1$ foliation. This is the justification for "editing" the modeled points. When points with low values of $\delta_3$ or $\kappa_{2:3}$ are excluded, the plotted poles of the edited points (Figure 17c) are in good qualitative agreement with Figure 17a. We color-coded points in Figures 17b and the associated site location map (Figure 17d) to identify points associated with low values of $\delta_3$ (yellow), $\kappa_{2:3}$ (green), or both (red). The remaining ("edited") points in Figure 17c are indicated in black on the site map. When the same points are used to form structure tensors $\Upsilon_{jk}$, the observed and modeled eigenproperties are also in good agreement (Table 2). Given that the specific locations of the field measurement sites for $S_1$ were not recorded, there can be no exact comparison between the measured and modeled

points. It is interesting that many of the acceptable sites (black dots in Figure 17d) for the modeled $S_1$ lie close to the flow centerline. This is consistent with the field observation (subsection 4.3) that the foliation was best developed close to the medial moraine.

### 5.4. Folding ($F_1$ and $F_3$)

At the 30 m×30 m scale of our ice dynamics model, folding is a sub-grid process so a direct attack on fold modeling is not feasible. Rather than attempt to model folds, we highlight the deformation conditions that favor the presence of folded ice. From this perspective, the deformation gradient tensor $F_{jk}$ holds promise because it measures accumulated strain and is closely associated with strain ellipsoids which are useful for visualizing rotation and strain stretching. However folds cannot be generated by stretching and rotation alone so $F_{jk}$ cannot capture the complexity that is required for folding. For this reason we propose that the gradient of the deformation gradient tensor $T_{ijk} = \partial F_{jk}/\partial x_i$ merits attention. On the downside, the $F_{jk}$ tensor is rank 2 and has 9 scalar components whereas $T_{ijk}$ is rank 3, has 27 scalar components, and is thus more cumbersome. With these considerations in mind, we suggest that one of the scalar invariants of $T_{ijk}$ (there are 12) could serve as a fold-propensity index. The scalar that we propose as a fold index to parameterize the prevalence of $F_3$ (Table 1) is $\mathcal{Q}_2 = T_{iji}T_{pjp}$. As previously stated, we adopt the Einstein summation convention for repeated subscripts so the fully-expanded expression is $\mathcal{Q}_2 = (T_{111} + T_{212} + T_{313})^2 + (T_{121} + T_{222} + T_{323})^2 + (T_{131} + T_{232} + T_{333})^2$. An attractive feature of scalar invariants is their independence on the coordinate system. Glaciologists are most familiar with the second invariant of the deviatoric stress tensor which appears in the generalized form of Glen's flow law [e.g., *Cuffey & Paterson*, 2010,

p. 59–60]. We continue this discussion and present an algorithm for calculating $T_{ijk}$ in *Clarke & Hambrey* [2019].

Figure 18 shows centerline profiles of $\log_{10} \mathcal{Q}_2$ for two versions of the Trapridge Glacier model, both observed at 2006.6. The upper panel is for the reference model, which assumes a 50-year surge cycle, and the lower panel is for a non-surging version of the same model ($\mathcal{C}_{\text{surge}}$=$\mathcal{C}_{\text{slide}}$). The plots correspond to where folds would be observed but not necessarily where they form. Warm colors indicate regions that are highly favorable for folds to exist and cool colors the opposite. Unsurprisingly, folds are expected to be found near the glacier bed, near bumps in bed topography, and toward the glacier terminus. Near the glacier terminus, folds that formed at depth can become exposed at the ice surface (Figure 6). Curiously the non-surging model indicates more intense folding than for the surging model, a result that is counter-intuitive but not necessarily incorrect. It could also point to shortcomings of the fold index parameterization.

The modeling effort required for evaluating $T_{ijk}$ at selected grid points is substantial and involves integrations along ice-particle trajectories. The accuracy of these integrations decreases near the bed and near the terminus. For this reason we have no reliable results for ice at the bed or near the terminus. The location of the centerline profiles is plotted in Figure 11.

Unfortunately the observed folds in Trapridge Glacier (Figure 6) are at the glacier terminus near the bed. Our model is incapable of calculating accurate trajectories for this ice and thus we have no information on $T_{ijk}$ or $\mathcal{Q}_2$ for this part of the glacier. Comparison between observed and modeled folding is therefore impossible. We know from an earlier field study [*Clarke & Blake*, 1991] that basal thrust features develop near the glacier

centerline and upflow from the ice terminus. So, at the very least, the modeled folding zone is where complex flow is known to occur.

### 5.5. High-angle Fractures and Veins ($S_4$)

In terms of field effort, the study of high-angle fractures and veins or crevasse traces (Figures 7, 8, 9, and 10) was the most demanding component of the structure study. For a combination of reasons, this also constitutes the greatest challenge for structure modeling. Glen's flow law and rheological models for glacier flow modeling assume that ice deforms like a viscous fluid. Thus conventional ice dynamics models can calculate the advection and rotation of fracture planes. However viscous fluids do not fracture so the description is incomplete. To circumvent this difficulty it is commonly assumed that the calculated viscous stresses can be applied, without modification, to ice that is assumed, on a shorter time scale, to behave as a linearly elastic solid. However, linear elastic solids do not fracture either, so, as a further step, a fracture stress criterion is invoked. The foregoing simplifications are standard ones and known as the linear elastic fracture model (LEFM) [e.g., *Smith*, 1976; *van der Veen*, 1998a, b].

In nature, once fracture has occurred, the fractured material is changed and stresses are rearranged. Whether existing fractures are extended or new fractures introduced is determined by the stress field in the damaged material; over time cracks can heal. None of this is treated in the LEFM. Furthermore, the ice dynamics model that we use is based on the shallow ice approximation [*Greve & Blatter*, 2009] which yields a less accurate solution for the stress field than might be achieved with a full stress model [e.g., *Gagliardini et al.*, 2013]. For the present study we are untroubled by this consideration. It is only one

of many shortcomings of the fracture modeling and unlikely to explain the differences between measured and modeled crevasse traces.

Another concern is the inconsistency between how crevasse traces are measured in the field and how they are treated within the model. For each case, the results of crevasse trace measurements are assigned to a point on the glacier surface but, in fact, the field observations are taken over an area of the surface (e.g., $50\,\mathrm{m}^2$ for the crack density measurements), then summed, and finally assigned to a point. In contrast, the model tracks the fate of a single ice particle as it passes through the glacier and records at each time step the velocity gradient $L_{jk}$, stress $\sigma_{jk}$, and other relevant fields at that point. Fracture is deemed to occur when conditions at the point satisfy specified fracture criteria. Over time, the point can be subjected to a sequence of fracture failures. In the model, a nearby point would experience a nearly identical record of fractures. In the field, a crack credited to a given measurement site (and hence to a given ice particle) might occur at some distance from the site and the crevasse traces are not concentrated at a single point. Indeed, if this were the case it would be near-impossible to measure them individually.

### 5.5.1. Stereoplots

Figure 19 shows the measured (as in Figure 8) and modeled crevasse traces for flow centerline and mound sites on Trapridge Glacier for the 2006.6 observation year. The "observed" (estimated from 2006.6 observations at the site) and modeled ice flow directions are indicated by arrow annotations. Agreement between estimated and modeled flow directions is best (within $\pm 3.5°$) for sites FC3, FC4, FC5, and M4 and worst for FC1 ($\pm 25.9°$) and FC7 ($\pm 26.7°$).

Comparison of the measured and modeled stereoplots and rose diagrams requires awareness of the shortcomings of each approach. It is simplest to compare like-with-like so we start by comparing the observed and modeled scatterplots (leftmost circles in each panel). The points represent lower hemisphere projections of poles of crevasse traces and the majority of these are near the circle perimeter, indicating that both the measured and modeled fracture planes are near-vertical. In this projection, points near the western edge correspond to planes that dip to the east and vice versa. A problem with this type of stereographic projection is that a small difference in the dip angle of the near-vertical planes can change the dip direction from west to east. This sensitivity to small differences influences both the scatterplots and the contoured plots of point density (middle circle in each panel) and must be recognized when observed and modeled result are compared. With this thought in mind the best agreement between the scatter- and contour plots is for sites FC1, FC2, FC4, and M4, and the worst for FC7 and M1.

The rose diagrams (rightmost circles in each panel) are two-dimensional and map the dip directions of crevasse traces. To avoid the problem of sensitivity to the dip direction, which afflicts the scatter- and contour plots, we treat dip directions as bipolar rather than unipolar, so that a northward or southward dip are both grouped as north–south and the resulting rose diagram has point symmetry about its center [as in *Hubbard & Glasser*, 2005]. Agreement between measured and modeled rose diagrams is quite good for FC2, FC3, and FC4; the slight disagreement between the measured and modeled alignments of patterns could result from differences between the true and modeled flow rotation. Larger alignment discrepancies are associated with FC1, FC5, and FC7.

The lack of success in modeling crevasse trace alignment can be largely or entirely attributed to the crack model and to the timing of surges. By examining modeled ice particle trajectories for each site (e.g., Figure 3 of *Clarke & Hambrey* [2019]) we found that, for most sites, crack damage is incurred near the start and endpoints of the flow trajectory when the ice particle is near the glacier surface. The depth of penetration of crevasses is an important consideration and we suspect that this depth varies over the surge cycle, being deepest when crevasses are isolated rather than closely-space and influenced by the availability of surface melt water.

### 5.5.2. Crack Counts and Crack Density

Figure 20 compares the observed (Figure 20a) and modeled (Figure 20b) crack counts for flow centerline and mound sites. Observed and modeled crack counts are not directly comparable. Field measurements yield crack counts within a $50\,m^2$ longitudinal swath at each site which is then applied to a "parcel" of ice, whereas the model accumulates the crack count experienced by a single ice particle. Thus the precise counts (and the vertical scales of the bar graphs) cannot be compared.

The most striking feature of the observed crack count is the unexpected tendency for the count to *decrease* from a maximum at FC2 (near the ELA) to much lower values at FC6 and FC7 near the terminus. This trend is highlighted by plotting crack count vs. downflow distance (Figure 21). The modeled variation of crack count with distance (Figure 21b) agrees surprisingly well with observations and provides an explanation for the apparent paradox: surface ice at downglacier sites follows a deeper trajectory than ice at upglacier sites such as FC2. Because tensile stresses decrease with depth, ice following a shallow trajectory, like that for FC2, is more fracture-prone than for a deep trajectory.

Despite the apparent success of the modeled crack counts for flow centerline sites there is a large disagreement between observed and modeled crack counts for the mound sites with the observations giving high crack counts and the model giving low counts.

We found the simulations of crack density to be strongly dependent on the ice fracture model; the Nye fracture criterion [*Nye*, 1957], which predicts shallow crevasse penetration, yields satisfactory results. An alternative model, suitable for isolated crevasses and yielding deeper penetration depths [e.g., *Smith*, 1976; *van der Veen*, 1998a, b], predicted a monotonically increasing crack density with distance. For Trapridge Glacier simulations, the Nye model is preferable because, as for other surging glaciers, crevasses tend to be closely-spaced rather than isolated. Out of interest, we also included simulations for a non-surging version ($\mathcal{C}_{\text{surge}} = \mathcal{C}_{\text{slide}}$) of the Trapridge model (Figure 20c) to examine whether crack production in a surging glacier differs substantially from that in a non-surging glacier. The modeled crack densities differ but not in a striking manner.

For both the measured and modeled results the crack counts are binned according to the observed crack orientations at the 2006.6 measurement sites. Cracks are classified as diagonal ($-70°<\Delta\vartheta<-20°$ or $20°<\Delta\vartheta<70°$), longitudinal ($-20°\leq\Delta\vartheta\leq+20°$), and transverse ($-90°\leq\Delta\vartheta\leq-70°$ or $+70°\leq\Delta\vartheta\leq90°$), relative to the inferred or model-calculated flow direction $\vartheta$. Both the observations and model agree that the crack count for longitudinal cracks is less than for transverse and diagonal cracks but, at most sites, the model greatly underestimates the frequency of longitudinal cracking. The crack model considers only Mode I (tensile) failure and allowing other failure modes might increase the crack diversity.

### 5.6. Transverse ($S_2$) Foliation

The field interpretation of the transverse $S_2$ foliation in section 4.4 suggests that the foliation originated as transverse near-vertical cracks that were subsequently compressed and vertically-rotated by flow to yield transverse structures having an upglacier dip. Additionally, the foliation was confined to the south flow unit (i.e., south of the medial moraine in Figure 14). Figure 22 shows simulated crack orientations for a line of sites in the south flow unit. For sites SL08 and SL09, 400–500 m far from the glacier terminus, the cracks tend to be near-vertical and not strongly oriented relative to the ice flow direction. At site SL10, roughly 200 m from the terminus there is a track of points that correspond to a set of crack planes having an upglacier dip, and roughly aligned transverse to the ice flow direction, matching the field description. At site SL11, the crack diagrams become very simple but continue to correspond to a set of crack planes, oriented transverse to flow and having an upglacier dip. The field description also noted that the structure consists of poorly defined anastomosing layers. These could result from the variable orientation and dip of crack planes, as for SL10.

## 6. Discussion

### 6.1. Observed Post-surge Structural Attributes

#### 6.1.1. Structural Sequence

Four phases of planar structure ($S_0$–$S_4$) and two phases of folding ($F_1$, $F_3$) were identified from three-dimensional analysis of the surface of the glacier and the ice-marginal cliff. They represent a sequence of structure-forming events that affect a "parcel" of ice as it moves through the glacier, although not all parts of the glacier are affected by all of the structures. In particular, the thrusts ($S_3$) and recumbent folds ($F_3$) affect only

the basal and intermediate depths within the glacier. A similar range of structures, though not necessarily in the same order of formation, has been recognized in surge-type polythermal glaciers in Svalbard, such as Bakaninbreen [*Hambrey et al.*, 1996] and in temperate Variegated Glacier in Alaska [*Lawson*, 1994].

### 6.1.2. Quiescent-phase Structural Development

Observations of the structure of Trapridge Glacier in 2006 allow discrimination of surge and non-surge attributes in a sequential context, and help to define how the surge front propagated through the glacier. Overall, the quiescent phase structures are longitudinal foliation and limited folding, which are evident at the glacier surface, but they are less obvious than structures that are attributed to surging. Within the main body of the glacier, especially where associated with the medial moraine, the foliation was probably formed where flow convergence took place in the upper reaches of the glacier, which in modeling we refer to as the "pinched model" [*Clarke & Hambrey*, 2019]. Because of the plug-flow nature of flow during the surge (evident in Figure 2), it is likely that foliation only formed during quiescent phase flow, except at the margins where strong shear prevailed during the surge. Flow-convergence results in large total strains, as a result of which the strain-ellipsoid, in disk-like form, becomes flattened in the plane of foliation. In other glaciers, e.g., Variegated Glacier, Alaska [*Lawson*, 1994] and Kongsvegen, Svalbard [*Glasser et al.*, 1998], $S_1$ has also been inferred to represent quiescent-phase deformation. Both these glaciers surge and the presence of the $S_1$ foliation is consistent with our model results that suggest that steady flow is not a requirement for the development of this foliation. An additional modification of foliation is localized distortion away from true flow-parallel configuration. *Fischer & Clarke* [1997a] observed that during the slow surge

of Trapridge Glacier, the glacier experienced stick–slip sliding behaviour as water pressure at the glacier bed varied. The development of "sticky spots" could explain why the foliation becomes distorted.

The hypothesis that there is a close correspondence between the plane of flattening of the strain ellipsoid and the plane of foliation is supported by the agreement between the observed and modeled stereoplots of the $S_1$ foliation (Figures 17a and 17c). Our association of the $S_1$ foliation with the quiescent phase is consistent with structure modeling results. For the Trapridge Glacier reference model, cumulative strain at 43 of 118 (36.4%) surface sites (Figure 17d favors formation of the $S_1$ foliation. For the same observation sites and a non-surging variant of the same model the percentage of favorable sites increases to 41.6%. The simplified models in *Clarke & Hambrey* (2019) show a similar tendency.

### 6.1.3. Surge Front Propagation and Associated Structures

The latest surge phase on Trapridge Glacier is exceptional for its slowness [*Frappé-Sénéclauze & Clarke*, 2007]. It is instructive to compare the structural attributes of the surge front with those of other glaciers. *Clarke & Blake* [1991] developed a number of surge-front models that showed various structural scenarios of propagation of the bulge, including recumbent folding of the glacier substrate, thrusting with debris, and the development of blind thrusts. Folding was discounted, and so was thrusting to the surface, as no surface manifestation of structures was apparent. The preferred mechanism was blind thrusting, whereby groups of thrusts were imbricated. These faults terminated at an edge-dislocation beyond which displacement was accommodated by creep deformation. The developing blind thrusts were indicated by growth on an internal sediment horizon

comprising basal debris between 1980 and 1988. Survey markers showed that propagation of the bulge was achieved by activation of the stagnant frontal apron. Longitudinal compression down-slope of the bulge caused the ice surface to rise, allowing the bulge profile to propagate in a continuous manner. The stagnant apron was incorporated into the bulge rather than overridden. Remnants of ice from the 1940s surge lasted into the mid-1980s and, for this surge, there was strong evidence of overriding.

Propagation of the surge front to the snout created a near-vertical cliff, which allowed the deep internal structure to be revealed for the first time. This enabled further development of a conceptual structural model to illustrate the propagation of the bulge to the snout (Figure 23). The original concept of blind thrusting is proved correct, but was accompanied by folding of basal ice containing subglacially derived debris (till). Thrusts propagate forwards from a basal décollement that is inferred to be the contact between the glacier and its bed of till. As these develop, downglacier-verging open folds, commonly laden with basal debris, grow into recumbent folds whose lower limbs may be sheared off by the developing thrusts. It has been suggested that the thrusts developed at the transition from wet-based ice to cold ice [*Clarke & Blake*, 1991], a mechanism also suggested for polythermal glaciers in Svalbard [*Hambrey et al.*, 1999]. Since an abundance of basally derived debris is associated with these thrusts, the initial entrainment of debris must be achieved by regelation and accretion of basal ice. This process probably occurred close to the thermal boundary between warm and cold-based ice. Once the stagnant ice apron had been over-run, and the surge front reached the snout, the topographic bulge steepened to a cliff, displaying all these structures clearly.

The key difference from the Svalbard glaciers is in the style of thrusting. All these other glaciers have prominent thrusts on their surface, which dip at moderate to high angles upglacier. In an example of investigations made during an actual surge, that of Bakaninbreen, was accompanied by movement through the glacier of a wall of fractured ice. This wall collapsed onto the stagnant ice in front, but also saw the development of a fore-bulge [*Murray & Booth*, 2010]. Following cessation of the surge, the cliff reduced to a ramp, displaying anastomosing thrusts, some of which showed signs of lubrication by abundant meltwater. This particular surge, however, stopped short of the snout. More recently the surge of partially tidewater Comfortlessbreen did not produce a prominent bulge, but saw advance of a heavily crevassed snout accompanied by high-angle thrusting and debris-entrainment in the terrestrial zone, and proglacial folding of marine sediments in the marine zone [*King et al.*, 2015]. In contrast, the slow surge of Trapridge Glacier produced thrusts which propagated from a bed that is inclined at approximately 7°, with an initial dip downglacier at an angle somewhat less than that of the bed. These thrusts barely attain an upglacier attitude when they intersect the ice cliff so that few, if any, of these thrusts intersected the glacier surface.

The fold model (Figure 18) contributes little to this discussion, in part because the modeled region and the sites where folds and thrusts were observed do not coincide. The larger problem is that the ice dynamics model lacks the resolution and the physics to represent folds and thrusts. Comparison of the fold intensity diagrams for surging and non-surging models of Trapridge Glacier, although hardly definitive, do not support the idea that surging glaciers have a greater tendency to construct folds than non-surging glaciers. Whatever the truth, it is likely that folds formed at the base of a glacier are

more readily observed in surging glaciers, in part because of the steep exposed ice faces that result from surges.

### 6.1.4. Crevasse Formation Following Passage of Surge Front

Crevasses and their traces provide evidence of the flow history of a glacier [*Herzfeld et al.*, 2004; *Colgan et al.*, 2016]. In non-surging glaciers, the development and distribution of brittle structures is controlled by mass balance and bed morphology [*Herbst et al.*, 2006]. In surging glaciers, changes in bed conditions lead to accelerated flow and crevasse development. During most glacier surges, following passage of the surge front, the glacier surface becomes totally crevassed, with many intersecting sets. Typical examples are Variegated Glacier, Alaska [*Lawson*, 1996] and Monacobreen, Svalbard [*Murray et al.*, 2003], which were both almost totally crevassed during their surges. In contrast, the slow surge of Trapridge Glacier revealed both crevassed and non-crevassed areas. However, crevasse traces are ubiquitous and much denser than on non-surging glaciers (up to 3 fractures per $m^2$; Figures 9 and 10), although no systematic measurements are available elsewhere for comparison. Most of these structures indicate that tensile strain-rates did not reach the threshold for crevasse initiation.

Crevasse traces, analysed in detail in key locations, did not yield consistent orientations in relation to the flow direction, as defined by the medial moraine. On examining fracture orientations along the flow-centerline we found one case where the majority of crevasse traces and crevasses had formed normal to the flow direction, as expected, but in other cases the orientations are bimodal or form broad girdles, when plotted on stereographic projections. Similarly, the surface mounds, which are thought to reflect protuberances in the glacier bed, had variably oriented crevasses, although generally at a higher density.

Individual sets of crevasse traces did not survive downglacier for more than a few hundred meters, suggesting that they only extended to a shallow depth when formed. This is in contrast to crevasse traces in non-surge-type glaciers, where they may extend downglacier for several kilometers, and even to the bed, as exemplified by Blue Glacier, Washington [*Allen et al.*, 1960], White Glacier, Nunavut, Canada [*Hambrey & Müller*, 1978] and Griesgletscher, Switzerland [*Hambrey and Milnes*, 1977].

The inconsistent nature of crevasse orientations is probably a reflection of a bed that is heterogeneous in terms of irregular topography, sedimentary facies composition, and hydraulic properties. The identification of stick-slip motion and presence of sticky spots that are temporally and spatially variable [*Fischer & Clarke*, 1997a] reinforces this view; such areas can lead to rotation of surface structures such as crevasse traces, as well as foliation.

## 7. Conclusions

The key observationally-based conclusions from this study are: (1) Trapridge Glacier has experienced two surges in the last 70 years, one in the 1940s that appears to have been a normal rapid surge, and a second slow surge that ended in 2005. (2) The earlier surge resulted in a totally crevassed glacier tongue that on melting back revealed dead ice with strong longitudinal foliation. (3) Subsequent quiescent-phase flow produced a near-pervasive longitudinal foliation in the newly active tongue. (4) The new phase of surging was accompanied by the development of a prominent bulge, which showed no surface manifestation of thrusting or recumbent folding; local distortion of the foliation was also evident. (5) Once the surge front reached the snout, the deeper internal structure was revealed. Thrusting indeed was evident, but thrusts were blind and few intersected

the glacier surface, although they became exposed in the ice cliff. (6) Recumbent isoclinal and similar folding is associated with thrusting, with the lower limbs of the folds in places showing shearing off by a thrust. (7) Folding and thrusting provide an effective way for subglacial debris and basal ice to be elevated to a high englacial position in the glacier. (8) Passage of the surge front resulted in heavy fracturing behind, both in terms of shallow open crevasses and crevasse traces, although this was not on the scale of the earlier surge, or as evidenced by other glacier surges. (9) Fractures have a predominantly transverse orientation, followed by diagonal and longitudinal. Fracture density attains a maximum of $3\,\mathrm{m}^{-2}$ in the areas investigated.

There seems little systematic preferred orientation of fractures in relation to flow direction. Observation on supraglacial ice mounds suggests that uneven bed morphology and variable stick–slip motion are the main influences on crevasse and crevasse trace orientation, combined with extending flow behind the surge front.

The key model-based conclusions from this study are: (1) Medial moraine patterns can be readily simulated using conventional particle tracking. For Trapridge Glacier, observed and simulated patterns are uncomplicated so that agreement between observed and modeled patterns is not a good test of model skill. (2) The $S_0$ stratification can be modeled using the assumption of isochronous layering and a semi-Lagrangian tracer method. (3) The $S_1$ longitudinal foliation appears to be associated with the orientation and flattening of strain ellipsoids and can be modeled by calculating ellipsoid parameters from the deformation gradient tensor $F_{jk}$. The agreement between the observed and modeled foliation is good but the glaciological processes that link ice strain with foliation development require further study. (4) Modeling results are consistent with the suggestion

that the $S_2$ transverse foliation results from compression and rotation of transverse near-vertical cracks. (5) At the scale of the simulation model, folding is a sub-grid process. We therefore introduced a scalar "fold propensity index" based on a scalar invariant of the gradient of the deformation gradient tensor. The idea of representing complicated deformation as a scalar parameter is new and merits additional study. (6) Our modeling represents a first attempt to simulate the orientation distribution of crevasse traces. The agreement between observations and simulations was unsatisfactory, most likely because of oversimplifications in the model. (7) Crack density simulations yielded an explanation for the counter-intuitive observation that the density of surface cracking has a decreasing trend in the downglacier direction.

To summarize, the greatest modeling successes were associated with efforts to simulate kinematic structures that depend on the flow velocity field and its derivatives. Efforts to simulate glacier folds and the density and orientation of crevasse traces, structures that involve processes that are not considered in current ice dynamics models, were less successful and highlight a direction for future effort. Nested models would allow selective high resolution of the processes that control folding and thrusting. Likewise, hybrid models such as that of *Gong et al.* (2018), which combines a finite-element full-Stokes thermomechanical flow model with a discrete-element treatment of ice fracture, hold promise.

This study has demonstrated that structural glaciology can provide insight concerning the manner by which surges propagate through a glacier. It can also provide, through analysis of basally derived debris uplifted to an englacial position, evidence of the bed condition and its heterogeneity. By comparison with other glaciers, it is evident that a

wide range of glaciotectonic processes are at work, leading to a range of structural styles, with that of Trapridge Glacier being particularly distinctive.

**Acknowledgments.** MJH acknowledges the award of a Visiting Professorship at the University of British Columbia. The field work and model development were supported by grants to GKCC from the Natural Sciences and Engineering Research Council of Canada. We thank Etienne Berthier, Eric de Giuli, and Andrew Schaeffer for help on Trapridge Glacier, Tom-Pierre Frappé-Sénéclauze for sharing insights and thesis data, and Evan Miles for assistance with georeferencing aerial photographs. Berthier also provided ice-marginal position data for the glacier tongue in 2006. Christian Schoof made significant recommendations at many stages of this research. The suggestions and constructive criticisms of reviewers Doug Benn and Darrel Swift and Editor-in-Chief Bryn Hubbard are greatly appreciated. All observational data are available in the figures and tables of this manuscript. The DEM of surface topography was downloaded from http://ftp.geogratis.gc.ca/pub/nrcan_rncan/elevation/cdem_mnec/115/cdem. Scripts and data files used to produce the modeling results and associated figures were placed in a GitHub repository and can be accessed at https://doi.org/10.5281/zenodo.1491931.

## References

Ahlmann, H. W. (1935). Contribution to the physics of glaciers. *Geographical Journal*, *86*(2), 97–107. https://www.jstor.org/stable/1786585

Allen, C. R., Kamb, W. B., Meier, M. F., & Sharp, R. P. (1960). Structure of the lower Blue Glacier, Washington. *Journal of Geology*, *68*, 601–625. https://doi.org/10.1086/626700

Blake, E. W., Clarke, G. K. C., & Gérin, M. C. (1992). Tools for examining subglacial bed deformation. *Journal of Glaciology*, *382*(130), 388–396. https://doi.org/10.3189/S0022143000002264

Blatter, H., & Hutter, K. (1991) Polythermal conditions in Arctic glaciers. *Journal of Glaciology*, *37*(126), 261–269. https://doi.org/10.3189/S0022143000007279

Clarke, G. K. C. (1996). Lumped-element analysis of subglacial hydraulic circuits. *Journal of Geophysical Research*, *101*(B8), 17,457-17,599. https://doi.org/10.1029/96JB01508

Clarke, G. K. C., & Blake, E. W. (1991). Geometric and thermal evolution of a surge-type glacier in its quiescent state: Trapridge Glacier, Yukon Territory, Canada, 1969–89. *Journal of Glaciology*, *37*(125), 158–169. https://doi.org/10.3189/s002214300004291x

Clarke, G. K C., & Hambrey, M. J. (2019). Structural evolution during cyclic glacier surges: 2. Numerical modeling. *Journal of Geophysical Research*, DOI: 10.1029/2018JF004870.

Clarke, G. K. C., & Marshall, S. J. (2002). Isotopic balance of the Greenland Ice Sheet: modelled concentrations of water isotopes from 30,000 BP to present. *Quaternary Science Reviews*, *21*, 419–430. https://doi.org/10.1016/S0277-3791(01)00111-1

Clarke, G. K. C., Nitsan, U., & Paterson, W. S. B. (1977). Strain heating and creep instability in glaciers and ice sheets. *Reviews of Geophysics*, *15*(2), 235–247. https://doi.org/10.1029/RG015i002p00235

Clarke, G. K. C., Collins, S. G., & Thompson, D. E. (1984). Flow, thermal structure and subglacial conditions of a surge-type glacier. *Canadian Journal of Earth Sciences*, *21*(2), 232–240. https://doi.org/10.1139/e84-024

Clarke, G. K. C., Anslow, F. S., Jarosch, A. H., Radić, V., Menounos, B., Bolch, T., & Berthier, E. (2013). Ice volume and subglacial topography for western Canadian glaciers from mass balance fields, thinning rates, and a bed stress model. *Journal of Climate*, *26*, 4282–4303. https://doi.org/10.1175/JCLI-D-12-00513.1

Clarke, G. K. C., Lhomme, N., & S. J. Marshall (2005). Tracer transport in the Greenland ice sheet: three-dimensional isotopic stratigraphy. *Quaternary Science Reviews*, *24*, 155–171. https://doi.org/10.1016/j.quascirev.2004.08.021

Colgan, W., Rajaram, H., Abdulati, W., McCutchan, C., Mottram, R., Moussavi, M. S., & Grigsby, S. (2016). Glacier crevasses: Observations, models, and mass balance implications. *Reviews of Geophysics*, *54*, 119–161, 10.1002/2015RG000504.

Collins, S. G. (1972). Survey of the Rusty Glacier area, Yukon Territory, Canada, 1967–70. *Journal of Glaciology*, *11*(62), 235–253. https://doi.org/10.3189/S0022143000022231

Cuffey, K. M., & Paterson, W. S. B. (2010). *The Physics of Glaciers* (4th ed.). Burlington: Elsevier. https://doi.org/10.3189/002214311798843412

Dowdeswell, J. A., & Lindsay Collin, R. (1990). Fast-flowing outlet glaciers on Svalbard ice caps. *Geology*, *18*, 778–781. https://doi.org/10.1130/0091-7613(1990)018¡0778:FFOGOS¿2.3.CO;2

Fischer, U. H., & Clarke, G. K. C. (1997a). Stick–slip sliding behaviour at the base of a glacier. *Annals of Glaciology*, *24*, 390–396. https://doi.org/10.3189/S0260305500012490

Fischer, U. H., & Clarke, G. K. C. (1997b). Clast collision frequency as an indicator of glacier sliding rate. *Journal of Glaciology*, *43*(145), 460–466. https://doi.org/10.3189/S002214300003505X

Fischer, U. H., Clarke, G. K. C., & Blatter, H. (1999). Evidence for a temporally varying "sticky spots" at the base of Trapridge Glacier, Yukon Territory, Canada. *Journal of Glaciology*, *45*(150), 352–360. https://doi.org/10.3189/S0022143000001854

Flowers, G. E., & Clarke, G. K. C. (1999). Surface and bed topography of Trapridge Glacier, Yukon Territory, Canada: digital elevation models and derived hydraulic geometry. *Journal of Glaciology*, *45*(149), 165–174. https://doi.org/10.1017/S0022143000003142

Flowers, G. E., & Clarke, G. K. C. (2000). An integrated modelling approach to understanding subglacial hydraulic release events. *Annals of Glaciology*, *31*, 222–228. https://doi.org/10.3189/172756400781820471

Flowers, G. E., & Clarke, G. K. C. (2002a). A multi-component coupled model of glacier hydrology: 1. Theory and synthetic examples. *Journal of Geophysical Research*, *107*(B11), 2287. https://doi.org/10.1029/2001JB001122

Flowers, G. E., & Clarke, G. K. C. (2002b). A multi-component coupled model of glacier hydrology: 2. Application to Trapridge Glacier, Yukon, Canada. *Journal of Geophysical Research*, *107*(B11), 2288. https://doi.org/10.1029/2001JB001124

Frappé-Sénéclauze, T.-P. (2006). Slow surge of Trapridge Glacier, Yukon Territory, 1951–2005 (MSc thesis). Vancouver: University of British Columbia.

Frappé-Sénéclauze, T.-P., & Clarke, G. K. C. (2007). Slow surge of Trapridge Glacier, Yukon Territory, Canada. *Journal of Geophysical Research*, *112*, F03S32. https://doi.org/10.1029/2006JF0040607

Gagliardini, O., Zwinger, T., Gillet-Chaulet, F., Durand, G., Favier, L., de Fleurian, B. ... Thies, J. (2013). Capabilities and performance of Elmer/Ice, a

new-generation ice sheet model. *Geoscientific Model Development*, *6*, 1299–1318, https://doi.org/10.5194/gmd-6-1299-2013

Glasser, N. F., Hambrey, M. J., Crawford, K., Bennett, M. R., & Huddart, D. (1998). The structural glaciology of Kongsvegen, Svalbard and its role in landform genesis. *Journal of Glaciology*, *44*(146), 136–148. https://doi.org/10.3189/S0022143000002422

Gong, Y., Zwinger, T., Åström, J., Altena, B., Schellenberger, T., Gladstone, R., & Moore, J. C. (2018). Simulating the roles of crevasse routing of surface water and basal friction on the surge evolution of Basin 3, Austfonna ice cap. *The Cryosphere*, *12*, 1563–1577. https://doi.org/10.5194/tc-12-1563-2018

Goodsell, R. C., Hambrey, M. J., Glasser, N. F., Nienow, P., & Mair, D. (2005). The structural glaciology of Haut Glacier d'Arolla, Valais, Switzerland. *Arctic, Antarctic, and Alpine Research*, *37*, 218–232. https://doi.org/10.1657/1523-0430(2005)037[0218:TSGOAT]2.0.CO;2

Greve, R., & Blatter, H. (2009). *Dynamics of Ice Sheets and Glaciers*. Berlin: Springer-Verlag

Hambrey, M. J. (1975). The origin of foliation in glaciers: evidence from some Norwegian examples. *Journal of Glaciology*, *14*(70), 181–185. https://doi.org/10.3189/S0022143000013496

Hambrey, M. J., & Milnes, A. G. (1977). Structural geology of an Alpine glacier (Griesgletscher, Valais, Switzerland). *Eclogae Geologicae Helvetiae*, *70*, 667–684.

Hambrey, M. J., & Müller, F. (1978). Ice deformation and structures in the White Glacier, Axel Heiberg Island, Northwest Territories, Canada. *Journal of Glaciology*, *20*(82), 41–66. https://doi.org/10.3189/S0022143000021213

Hambrey, M. J., Dowdeswell, J. A., Murray, T., & Porter, P. R. (1996). Thrusting and debris-entrainment in a surging glacier, Bakaninbreen, Svalbard. *Annals of Glaciology*, *22*, 241–248. https://doi.org/10.3189/1996AoG22-1-241-248

Hambrey, M. J., Bennett, M. R., Dowdeswell, J. A., Glasser, N. F., & Huddart, D. (1999). Debris entrainment and transfer in polythermal valley glaciers. *Journal of Glaciology* *45*(149), 69–86. https://doi.org/10.1017/S0022143000003051

Hambrey, M. J., Murray, T., Glasser, N. F., Hubbard, A., Hubbard, B., Stuart, G., ... Kohler, J. (2005). Structure and changing dynamics of a polythermal valley glacier on a centennial time-scale: Midre Lovénbreen, Svalbard. *Journal of Geophysical Research*, F010006. https://doi.org/10.1029/2004JF000128

Herbst, P., Neubauer, F., & Martin, M. P. J. (2006). The development of brittle structures in an alpine valley glacier: Pasterzenkees, Austria, 1887–1997. *Journal of Glaciology*, *52*(176), 128–136. https://doi.org/10.3189/172756506781828872

Herzfeld, U. C., Clarke, G. K. C., Mayer, H., & Greve, R. (2004). Derivation of deformation characteristics in fast-moving glaciers. *Computers & Geosciences*, *30*, 291–302. https://doi.org/10.1016/j.cageo.2003.10.012

Hooke, R. LeB., & Hudleston, P. J. (1978). Origin of foliation in glaciers. *Journal of Glaciology*, *20*(83), 285–299. https://doi.org/10.3189/S0022143000013848

Hubbard, B., & Glasser, N. (2005). *Field Techniques in Glaciology and Glacial Geomorphology*. Chichester: John Wiley.

Hubbard, A., & Hubbard, B. (2000). The potential contribution of high-resolution glacier flow modelling to structural glaciology. *Geological Society, London, Special Publications*, *176*, 135–146. https://doi.org/10.1144/GSL.SP.2000.176.01.10

Hudleston, P. J., & Hooke, R. LeB. (1980). Cumulative deformation in the barnes ice cap and implications for the development of foliation. *Tectonophysics*, *66*(1–3), 127–146. https://doi.org/10.1016/0040-1951(80)90042-6

Jarvis, G. T., & Clarke, G. K. C. (1975). The thermal regime of Trapridge Glacier and its relevance to glacier surging. *Journal of Glaciology*, *14*(71), 235–250. https://doi.org/10.3189/S0022143000021729

Jennings, S. J. A., Hambrey, M. J., & Glasser, N. F. (2014). Ice flow-unit influence on glacier structure, debris entrainment and transport. *Earth Surface Processes and Landforms*. *39*(10), 1279–1292. https://doi.org/10.1002/esp.3521.

Jennings, S. J. A, Hambrey, M. J., Glasser, N. F., James, T. D., & Hubbard, B. (2015). Structural glaciology of Austre Brøggerbreen, northwest Svalbard. *Journal of Maps*, *12*, 790–796. https://doi.org/10.1080/17445647.2015.1076744

King, O., Hambrey, M. J., Irvine-Fynn, T. D. L., & Holt, T. O. (2015). The structural, geometric and volumetric changes of a polythermal Arctic glacier during a surge cycle: Comfortlessbreen, Svalbard. *Earth Surface Processes and Landforms*, *41*, 162–177. https://doi.org/10.1002/esp.3796

Lawson, W. (1996). Structural evolution of Variegated Glacier, Alaska, U.S.A., since 1948. *Journal of Glaciology*, *42*(141), 261–270. https://doi.org/10.3189/S0022143000004123

Lawson, W. L., Sharp, M. J., & Hambrey, M. J. (1994). The structural geology of a surge-type glacier. *Journal of Structural Geology*, *16*(10), 1447–1462. https://doi.org/10.1016/0191-8141(94)90008-6

Lhomme, N., Clarke, G. K. C., & Marshall, S. J. (2005). Tracer transport in the Greenland Ice Sheet: constraints on ice cores and glacial history. *Quaternary Science Reviews*, *24*,

173–194. https://doi.org/10.1016/j.quascirev.2004.08.020

Lovell, H., Fleming, E. J., Benn, D. I., Hubbard, B., Lukas, S., & Naegeli, K. (2015a). Former dynamic behavior of a cold-based valley glacier on Svalbard revealed by basal ice and structural glaciology investigations. *Journal of Glaciology*, *61*(226), 309–328. https://doi.org/10.3189/2015JoG14J120

Lovell, H., Fleming, E. J., Benn, D. I., Hubbard, B., Lukas, S., Rea, B. R., ... Flink, A. E. (2015b). Debris entrainment and landform genesis during tidewater glacier surges. *Journal of Geophysical Research*, *120*(8), 1574–1595. https://doi.org/10.1002/2015JF003509

Murray, T., & Booth, A. D. (2010). Imaging glacial sediment inclusions in 3-D using ground penetrating radar at Kongsvegen, Svalbard. *Journal of Quaternary Science*, *25*, 754–761, https://doi.org/10.1002/jqs.1351

Murray, T., & Clarke, G. K. C. (1995). Black-box modeling of the subglacial water system. *Journal of Geophysical Research*, *100*(B6), 10,231–10,245. https://doi.org/10.1029/95JB00671

Murray, T., Stuart, G. W., Miller, P. J., Woodward, J., Smith, A. M., Porter, P. R., & Jiskoot, H. (2000). Glacier surge propagation by thermal evolution at the bed. *Journal of Geophysical Research*, *105*(B6), 13,491–13,507. https://doi.org/10.1029/2000JB900066

Murray, T., Strozzi, T., Luckman, A., Jiskoot., H., & Christakos, P. (2003). Is there a single surge mechanism? Contrasts between glacier surges in Svalbard and other regions. *Journal of Geophysical Research*, *108*(B5), 2237. https://doi.org/10.1029/2002JB001906

Nye, J. F. (1957). The distribution of stress and velocity in glaciers and ice sheets. *Proceedings of the Royal Society A: Mathematical, Physical and Engineering Sciences*, *23*(1216),

113–133. https://doi.org/10.1098/rspa.1957.0026

Sevestre, H., Benn, D. I., Luckman, A., Nuth, C., Kohler, J., Lindbåck, K., & Pettersson, R. (2018). Tidewater glacier surges initiated at the terminus. *Journal of Geophysical Research*, *123*(5), 1035–1051. https://doi.org/10.1029/2017JF004358

Smith, R. A. (1976). The application of fracture mechanics to the problem of crevasse penetration. *Journal of Glaciology*, *17*(76), 223–228. https://doi.org/10.3189/S0022143000013563

Stone, D. B., & Clarke, G. K. C. (1993). Estimation of subglacial hydraulic properties from induced changes in basal water pressure: a theoretical framework for borehole-response tests. *Journal of Glaciology*, *39*(132), 327–340. https://doi.org/10.3189/S0022143000015999

Stone, D. B., Clarke, G. K. C., & Ellis, R. G. (1997). Inversion of borehole-response test data for estimation of subglacial hydraulic properties. *Journal of Glaciology*, *43*(143), 103–113. https://doi.org/10.3189/S0022143000002860

van der Veen, C. J. (1998a). Fracture mechanics approach to penetration of surface crevasses on glaciers. *Cold Regions Science and Technology*, *27*, 31–47. https://doi.org/10.1016/S0165-232X(97)00022-0

van der Veen, C. (1998b). Fracture mechanics approach to penetration of bottom crevasses on glaciers. *Cold Regions Science and Technology*, *27*, 213–223. https://doi.org/10.1016/S0165-232X(98)00006-8

Woodward, J., Murray, T., & McCaig, A. (2002). Formation and reorientation of structures in the surge-type glacier Kongsvegen, Svalbard. *Journal of Quaternary Science*, *17*(3), 201–209. https://doi.org/10.1002/jqs.673

**Table 1.** Summary of structures in Trapridge Glacier in order of progressive downglacier development, using standard structural geological notation of S for planar structures and F for fold axes.

| Notation | Description | Structural interpretation |
|---|---|---|
| $S_0$ | Continuous, wavy, weakly developed gently dipping layers of coarse bubbly ice and thin clear ice, best exposed in crevasse walls, especially in upper ablation area | Stratification |
| $S_1$ | Longitudinally oriented, near-vertical intercalating layers of bubble-rich and bubble-poor ice, commonly defined by bubble elongation; variable strength across the width of the glacier tongue | Longitudinal foliation resulting from simple shear |
| $S_2$ | Limited distribution in south flow unit; weak anastomosing layers dipping moderately (30-50°) up glacier | Transverse foliation derived from crevasse traces |
| $S_3$ | Low-angle fractures in marginal cliff, extending for several tens of meters, commonly associated with basal debris | Thrusts connecting to glacier bed |
| $S_4$ | Clearly defined fractures and veins from $< 1$ cm to $> 1$ m wide, comprising clear ice crystals elongated normal to trace | Crevasse traces |
| $F_1$ | Low-amplitude dm-scale semi-continuous folds of layers of coarse bubbly ice (dominant) and coarse clear ice; higher amplitude similar-style folding with axial plane foliation in places; fold axes dip gently upglacier and are parallel to flow | Folded stratification |
| $F_3$ | Prominent meter-scale folding of debris of basal origin and coarse bubbly ice into isoclinal and similar-style forms; lower limbs commonly sheared off by $S_4$ structures; axes horizontal and sub-parallel to snout | Recumbent folds associated with thrusts |

**Table 2.** Observed and modeled eigenproperties of $S_1$ foliation at lower Trapridge Glacier sites for 2006.6

| Site | $k$ | $\lambda_k$ | $\mathbf{N}_k$ | | |
|---|---|---|---|---|---|
| | | | $N_x$ | $N_y$ | $N_z$ |
| Observed | 1 | 0.890 | −0.064 | −0.995 | 0.081 |
| | 2 | 0.087 | −0.997 | 0.059 | −0.059 |
| | 3 | 0.023 | −0.054 | 0.084 | 0.995 |
| Modeled | 1 | 0.742 | −0.123 | 0.990 | −0.073 |
| | 2 | 0.187 | 0.045 | 0.079 | 0.996 |
| | 3 | 0.071 | 0.991 | 0.119 | −0.055 |
| Edited | 1 | 0.896 | −0.159 | 0.987 | −0.028 |
| | 2 | 0.062 | −0.987 | −0.160 | −0.031 |
| | 3 | 0.042 | −0.035 | 0.022 | 0.999 |

**Table 3.** Modeled strain ellipsoids for Trapridge Glacier reference (surging) model and sites at 2006.6

| Site | Deposition date | $k$ | $\lambda_k^{\mathbf{V}}$ | $\mathbf{N}_k^{\mathbf{V}}$ | | | Axis ratios | | Dip |
|---|---|---|---|---|---|---|---|---|---|
| | | | | $N_x^{\mathbf{V}}$ | $N_y^{\mathbf{V}}$ | $N_z^{\mathbf{V}}$ | $\kappa_{1:2}$ | $\kappa_{2:3}$ | $\delta_3$ |
| FC1 | 1986.4 | 1 | 1.397 | 0.257 | −0.278 | 0.926 | 1.10 | 2.24 | 86.7 |
| | | 2 | 1.267 | 0.508 | −0.776 | −0.374 | | | |
| | | 3 | 0.565 | 0.822 | 0.566 | −0.058 | | | |
| FC2 | 1967.9 | 1 | 3.738 | 0.990 | 0.028 | −0.135 | 3.88 | 3.47 | 87.0 |
| | | 2 | 0.964 | 0.137 | −0.048 | 0.989 | | | |
| | | 3 | 0.278 | 0.021 | −0.998 | −0.052 | | | |
| FC3 | 1956.8 | 1 | 4.004 | 0.922 | 0.008 | 0.387 | 1.45 | 30.67 | 89.5 |
| | | 2 | 2.768 | −0.387 | −0.012 | 0.922 | | | |
| | | 3 | 0.090 | 0.012 | −1.000 | −0.008 | | | |
| FC4 | 1924.1 | 1 | 4.006 | −0.915 | −0.256 | −0.311 | 2.81 | 8.15 | 89.5 |
| | | 2 | 1.426 | −0.296 | −0.093 | 0.950 | | | |
| | | 3 | 0.175 | −0.272 | 0.962 | 0.010 | | | |
| FC5 | 1899.0 | 1 | 7.026 | 0.962 | 0.272 | −0.010 | 6.65 | 7.85 | 84.1 |
| | | 2 | 1.057 | 0.037 | −0.097 | 0.995 | | | |
| | | 3 | 0.135 | 0.270 | −0.957 | −0.104 | | | |
| FC6 | 1865.3 | 1 | 9.608 | −0.970 | −0.231 | 0.079 | 16.40 | 3.30 | 83.2 |
| | | 2 | 0.586 | 0.049 | 0.134 | 0.990 | | | |
| | | 3 | 0.178 | 0.239 | −0.964 | 0.119 | | | |
| FC7 | 1836.2 | 1 | 13.377 | −0.915 | 0.400 | −0.044 | 29.47 | 2.76 | 44.8 |
| | | 2 | 0.454 | −0.313 | −0.639 | 0.703 | | | |
| | | 3 | 0.165 | 0.254 | 0.657 | 0.710 | | | |

**Table 3.** Continued: Modeled strain ellipsoids for Trapridge Glacier reference (surging) model and sites at 2006.6

| Site | Deposition date | $k$ | $\lambda_k^{\mathbf{V}}$ | $\mathbf{N}_k^{\mathbf{V}}$ | | | Axis ratios | | Dip |
|---|---|---|---|---|---|---|---|---|---|
| | | | | $N_x^{\mathbf{V}}$ | $N_y^{\mathbf{V}}$ | $N_z^{\mathbf{V}}$ | $\kappa_{1:2}$ | $\kappa_{2:3}$ | $\delta_3$ |
| M1 | 1910.7 | 1 | 6.939 | −0.974 | 0.146 | −0.175 | 14.84 | 1.52 | 49.7 |
| | | 2 | 0.468 | −0.227 | −0.630 | 0.742 | | | |
| | | 3 | 0.308 | −0.002 | 0.762 | 0.647 | | | |
| M2 | 1883.4 | 1 | 8.819 | 0.989 | 0.148 | 0.013 | 19.61 | 1.78 | 13.2 |
| | | 2 | 0.450 | 0.022 | −0.228 | 0.973 | | | |
| | | 3 | 0.252 | 0.147 | −0.962 | −0.229 | | | |
| M3 | 1916.8 | 1 | 6.395 | 0.819 | 0.148 | 0.555 | 6.98 | 5.37 | 83.3 |
| | | 3 | 0.171 | 0.099 | −0.988 | 0.117 | | | |
| M4 | 1934.9 | 1 | 3.376 | −0.845 | −0.118 | −0.522 | 2.36 | 6.90 | 89.2 |
| | | 2 | 1.429 | −0.514 | −0.090 | 0.853 | | | |
| | | 3 | 0.207 | −0.148 | 0.989 | 0.015 | | | |

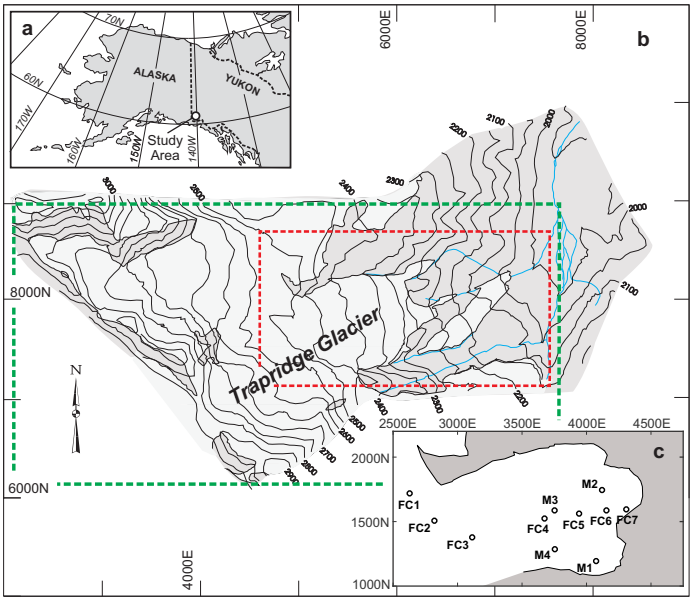


**Figure 1.** Location map for Trapridge Glacier study area in Yukon, Canada. (a) Study area near Alaska–Yukon border. (b) Map of Trapridge Glacier based on 1981 vertical aerial photography (e.g., Figure 2d). In the Zone 7 NAD27 UTM coordinate system used for this map the southwest corner (2000E, 6000N) corresponds to the UTM coordinates (532000E, 6786000N). (c) Map of measurement sites on lower Trapridge Glacier, with FC samples representing flow centerline and M the ice-surface mounds. The green-dashed outline gives the map limits of the computer model and the red-dashed outline the map limits of the site map (c). The model domain and the site map use the same coordinate system and the (0E,0N) origin of the model domain is at UTM (532105E, 6786145N).

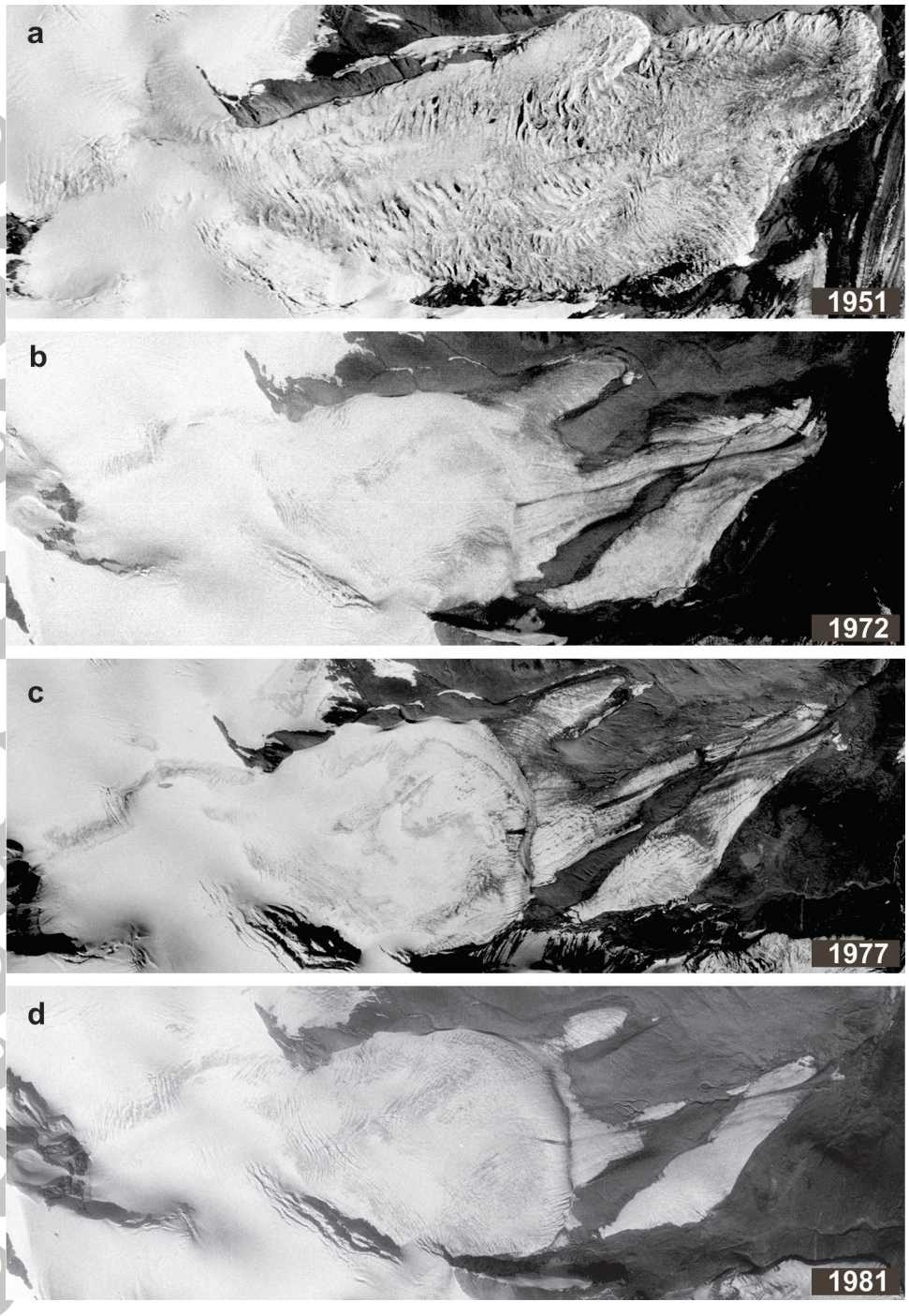


**Figure 2.** Series of aerial photographs of Trapridge Glacier over a 30 year period showing the 1940s surge followed by subsequent stagnation, increasing debris cover, and the progressive development of a new surge front (National Air Photo Library of Natural Resources Canada). (a) Post-1940s heavily crevassed and advanced surge condition (1951), (b) 1972. (c) 1977. (d) 1981.

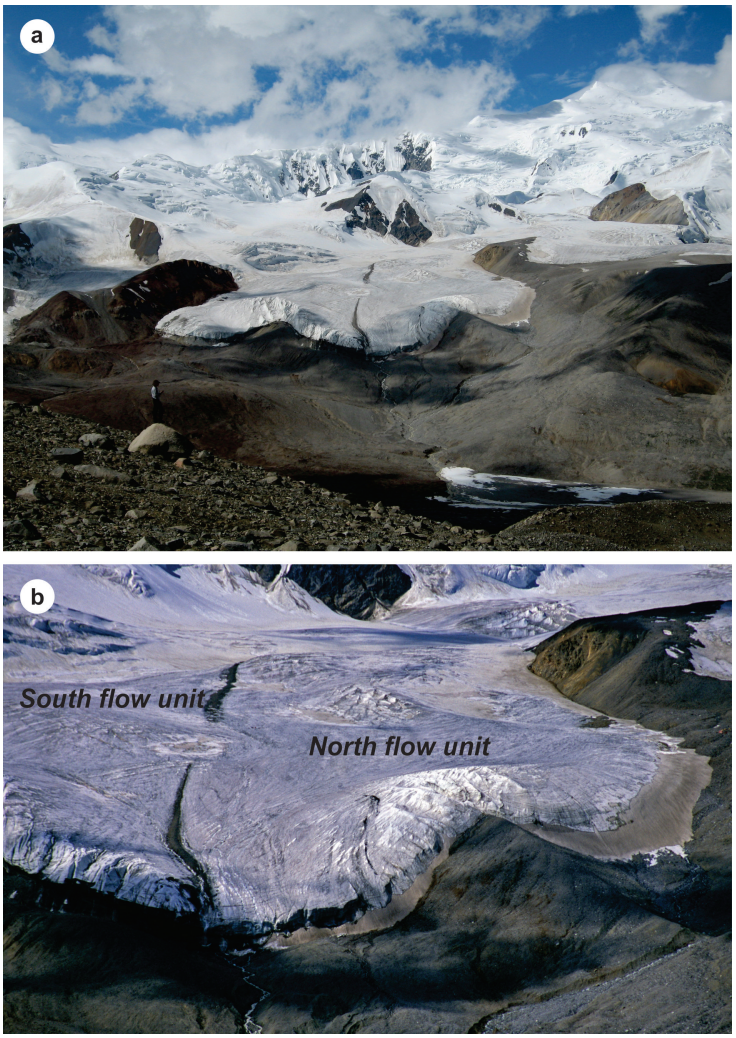


**Figure 3.** Trapridge Glacier tongue viewed from the northeast in August 2006. (a) General view with Mount Wood in the background and the terminal cliff that developed as the surge front reached the snout in the preceding year. (b) Telephotograph from the same location showing terminal cliff detail and glacier surface mounds, related to elevated areas of the glacier bed.

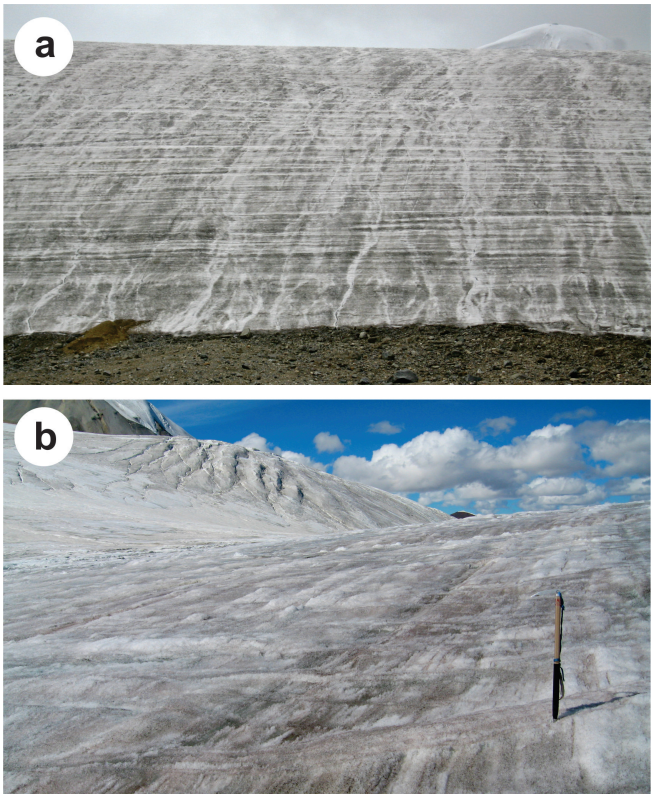


**Figure 4.** Primary stratification and foliation in Trapridge Glacier. (a) Well-developed near-horizontal stratification ($S_0$) exposed in the steep terminus of the northern arm just below the accumulation area. (b) Close-up of longitudinal foliation ($S_1$), intersected by crevasse traces ($S_3$) just below the equilibrium line in the northern flow unit.

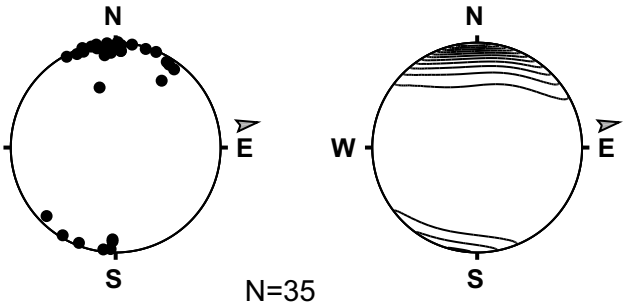


**Figure 5.** Equal-area, lower hemisphere projections of poles to longitudinal foliation $S_1$ in the tongue of Trapridge Glacier, illustrating the relationship with average flow direction denoted by the medial moraine. Arrows (roughly eastward-pointing) indicate the ice flow direction. Eigenvalues and eigenvectors calculated from points in the scatterplot are given in Table 2.

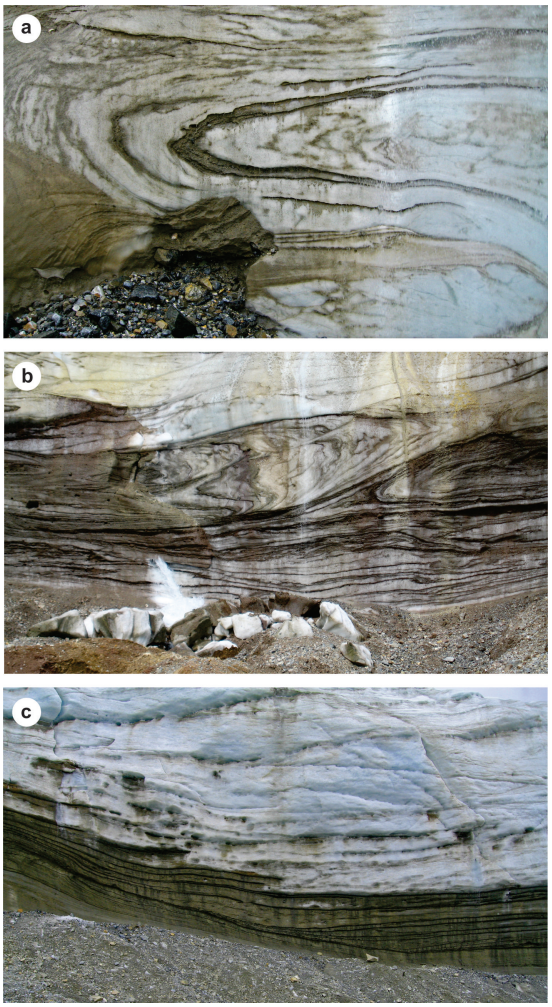


**Figure 6.** Deformation in the basal zone of Trapridge Glacier, where the surge front coincides with the glacier snout. (a) Detail of 2-m amplitude similar-style recumbent fold, comprising glacier ice and debris-rich basal ice; decimeter-scale parasitic folds are evident on the limbs of the main fold. (b) Complex recumbent isoclinal folding longitudinal foliation ($F_4$) in transverse section near true right margin of glacier; note that the lower limb of the main fold has its lower limb sheared off by a thrust ($S_4$); section about 5 m high. (c) Typical geometry of low-angle thrusts ($S_4$) with basal debris in mid-snout; note how they propagate from a lower thrust, and that some are blind; section about 5 m high.

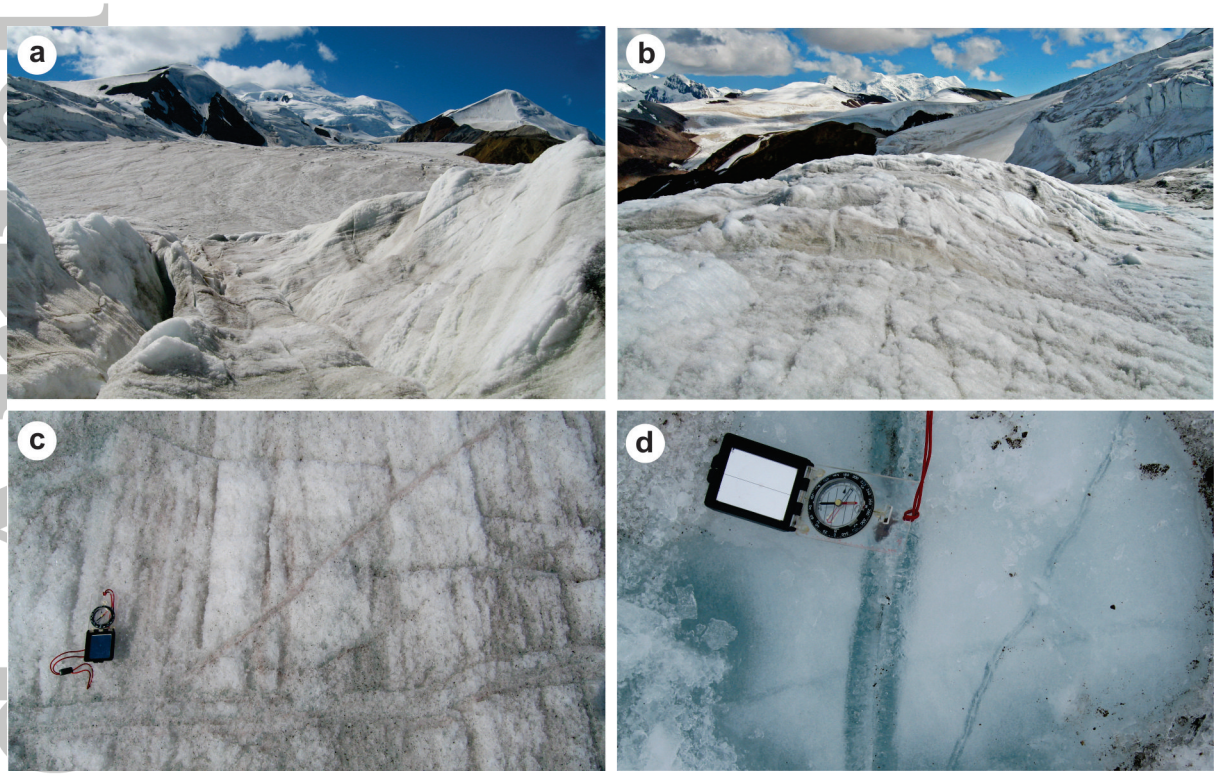


**Figure 7.** Fracture characteristics of Trapridge Glacier. (a) Narrow open and partly ablated longitudinal crevasse zone near snout of glacier, looking upglacier. (b) Glacier surface mound intersected by numerous short crevasse traces (predominantly transverse); downglacier to left. (c) Transverse and diagonal crevasse traces ($S_3$), intersecting longitudinal foliation ($S_1$); compass/clinometer for scale. (d) Cleaned and washed ice surface exposing internal structure of crevasse traces, including columnar crystal growth of coarse clear ice joining at a central suture, and cutting coarse bubbly glacier ice.

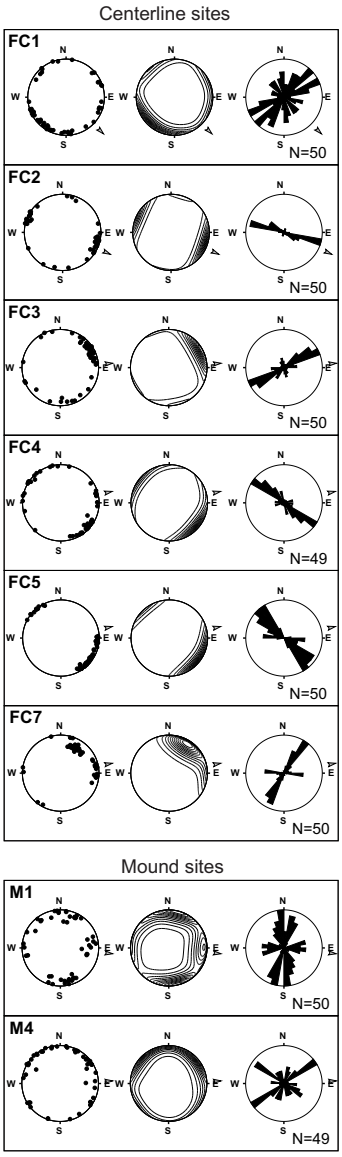


**Figure 8.** Crevasse trace measurements for FC (flow centerline) and M (mound) sites on Trapridge Glacier. Each panel presents measurement results in the form of a Schmidt diagram (equal-area, lower hemisphere projections of poles of crevasse traces), a contoured density plot of the same data, and a rose diagram of the dip directions of the crevasse traces. The observation year is 2006.6.

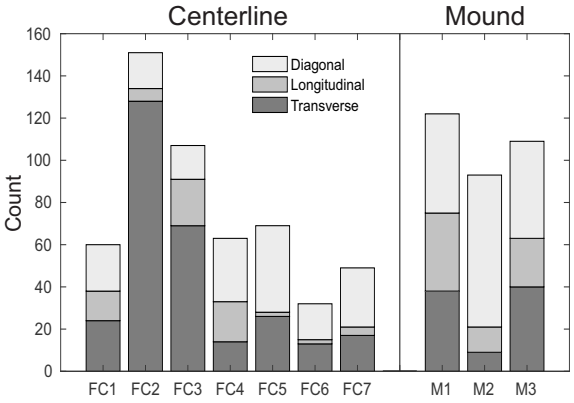


**Figure 9.** Observed crack count for flow centerline (FC) and surface mound (M) sites on Trapridge Glacier. For each site the sampled area is $50\,\mathrm{m}^2$ so crack density is simply the count divided by this area. The observation year is 2006.6.

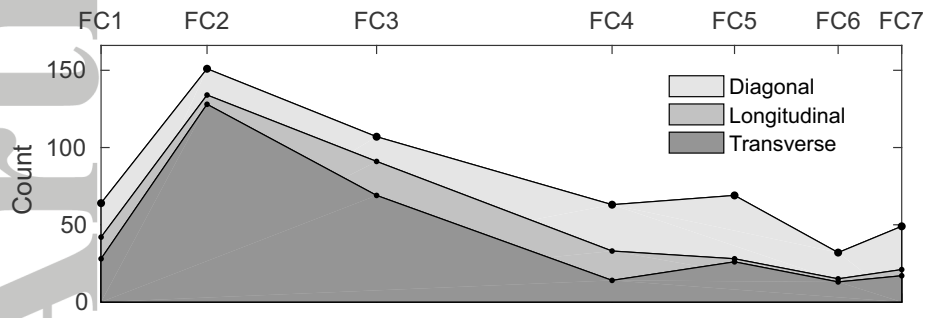


**Figure 10.** Observed crack count along flow centerline (FC) of Trapridge Glacier. For each site the sampled area is $50\,\mathrm{m}^2$ so crack density is simply the count divided by this area. The observation year is 2006.6.

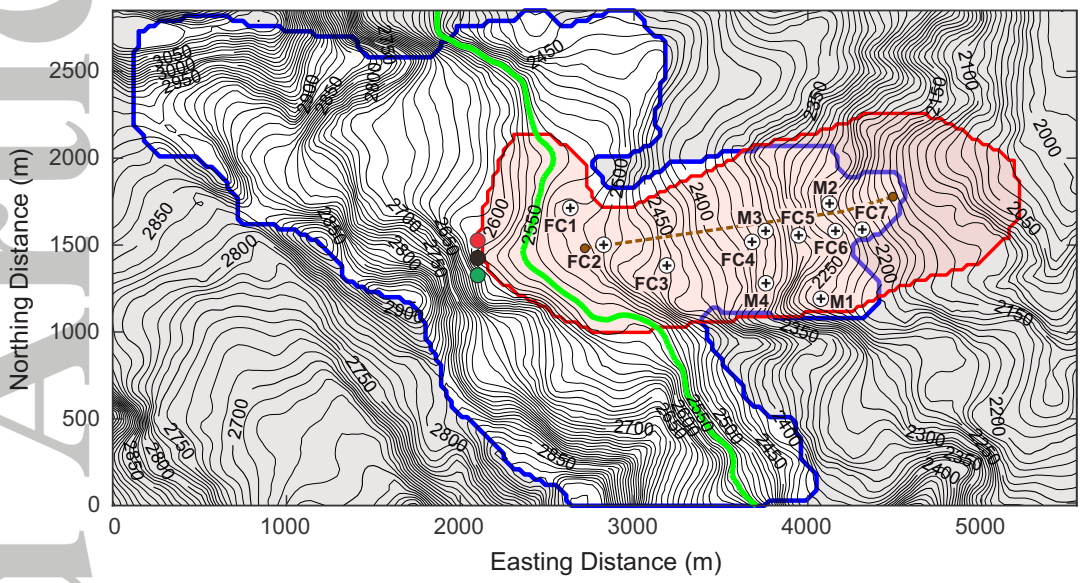


**Figure 11.** Reference map for Trapridge Glacier model with topographic and subglacial bed contours. The origin of the NAD27 UTM coordinate system (southwest corner point) is at (532105E, 6786145N). The glacier outline (blue) is calculated from the glacier dynamics model for the observation year 2006.6. The prescribed ELA for the ice dynamics model is indicated by a green line. Measurement sites are labeled FC1, FC2, etc. Pink shading indicates the assumed limits of the fast-sliding zone during surges. Solid circles in red, black and green near the western boundary of the fast-sliding zone indicate points at which morainal debris is introduced for numerical modeling of the medial moraine pattern. The profile line along which fold intensity is simulated is plotted as a brown-dashed line terminated by brown-filled circles.

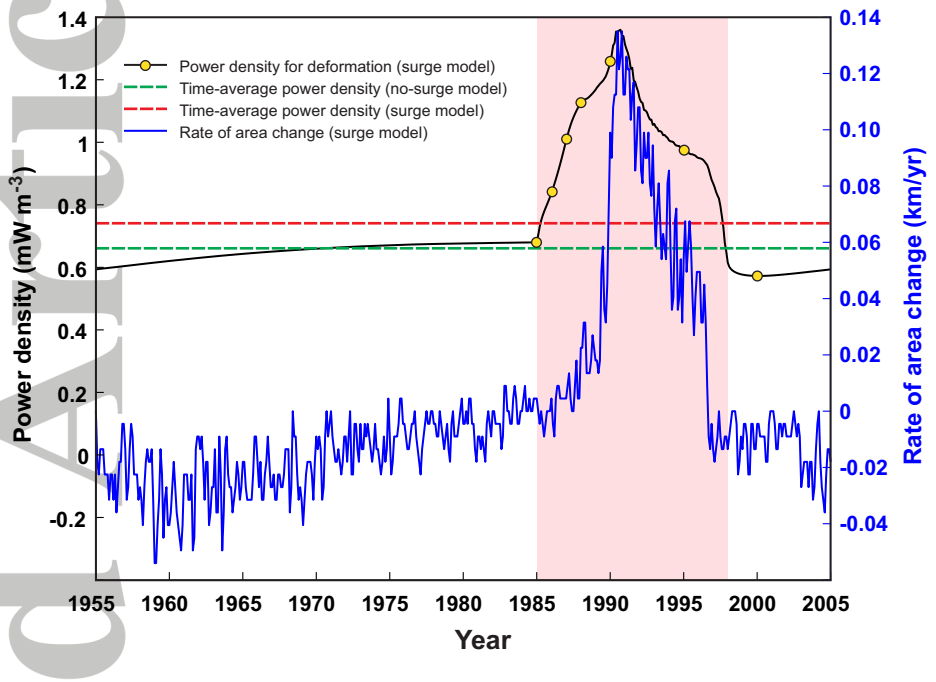


**Figure 12.** Time series for modeled deformational power density and rate of area change through a 50-year surge cycle. The pink background isolates the 13-year active phase of the surge during which the power density (black curve) and rate of change of area (blue curve) increase dramatically. Yellow circular markers on the power density plot indicate snapshot times for the sequence of maps in Figure 13. The time-averaged power density for the surging glacier model (dashed red line) and power density for a non-surging model of the same glacier (green-dashed line) differ only slightly.

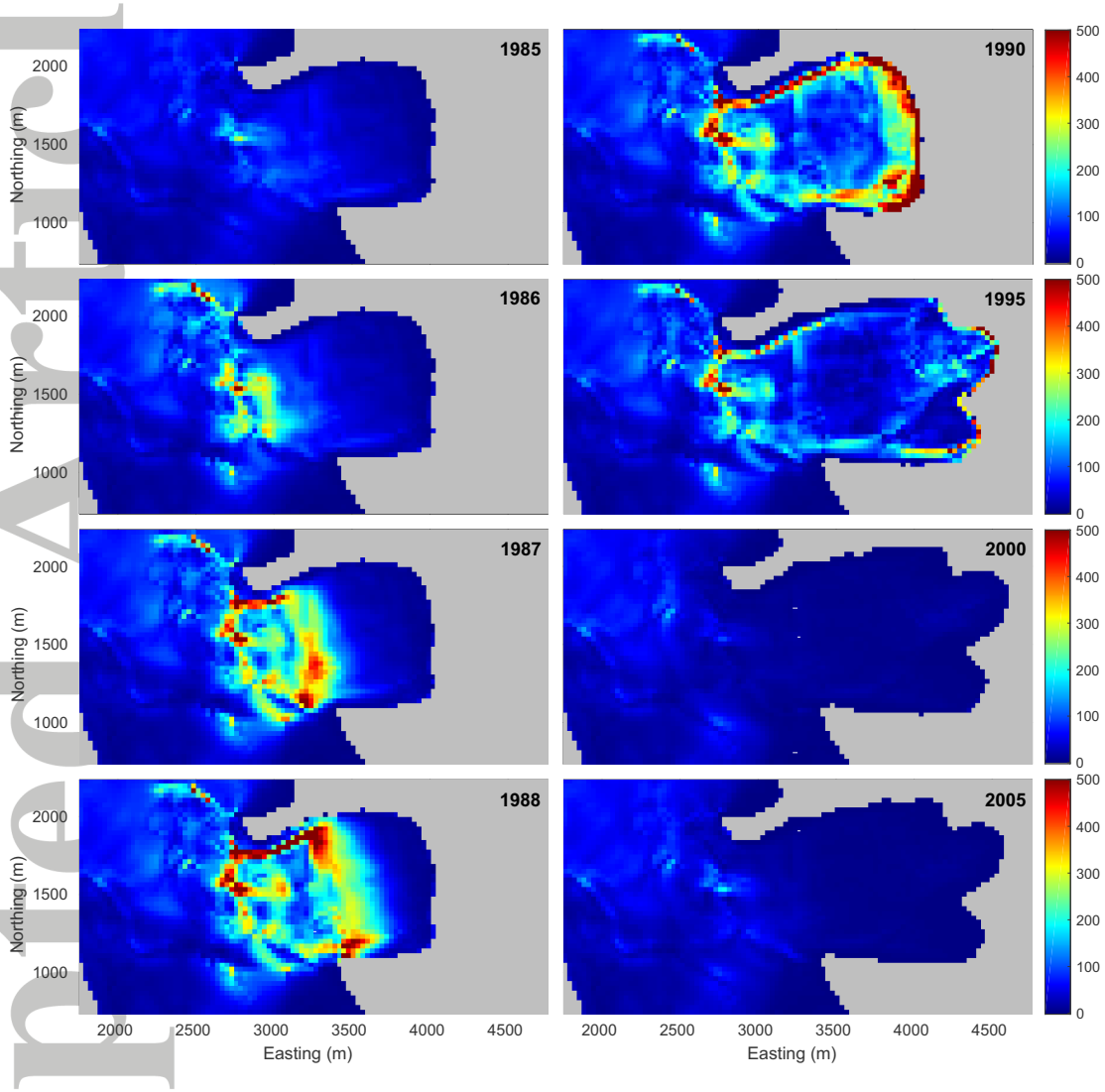


**Figure 13.** Maps of the vertically-integrated deformational power density at various times in the surge cycle. The 1985 snapshot corresponds to the surge onset; 1986, 1987, 1988 correspond to the 3-year accelerating phase of the surge; 1990 and 1995 to the contuing surge. The 2-year decelerating phase from 1996–1998 is not shown; post-surge snapshots for 2000 and 2005 complete the cycle.

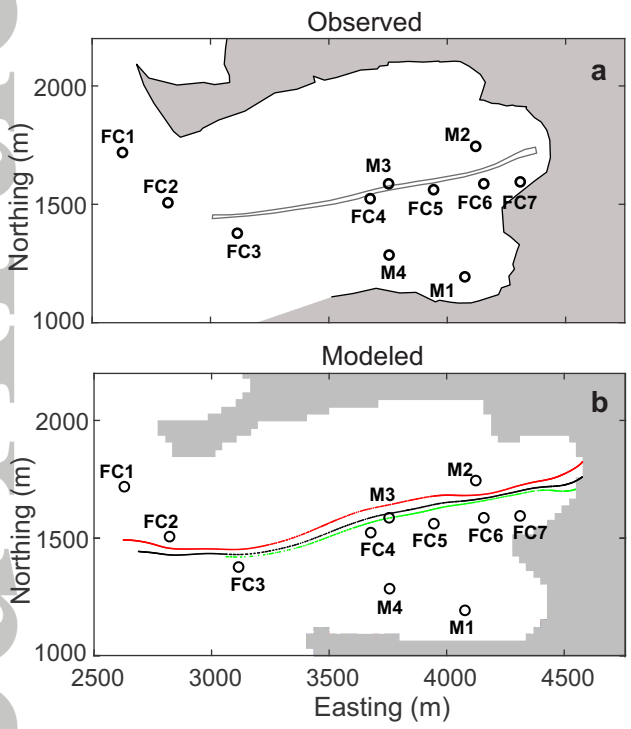


**Figure 14.** Observed and simulated medial moraine. (a) Map of lower part of Trapridge Glacier showing the 2006 ice margin as determined by Etienne Berthier, the sampling sites, and a sketch map of the medial moraine position in July 2006. (b) Simulated glacier extent and medial moraine position for 2006.6. Locations of the debris input points for the simulated moraine tracks (red, black, and green) are indicated by red, black, and green markers in Figure 11.

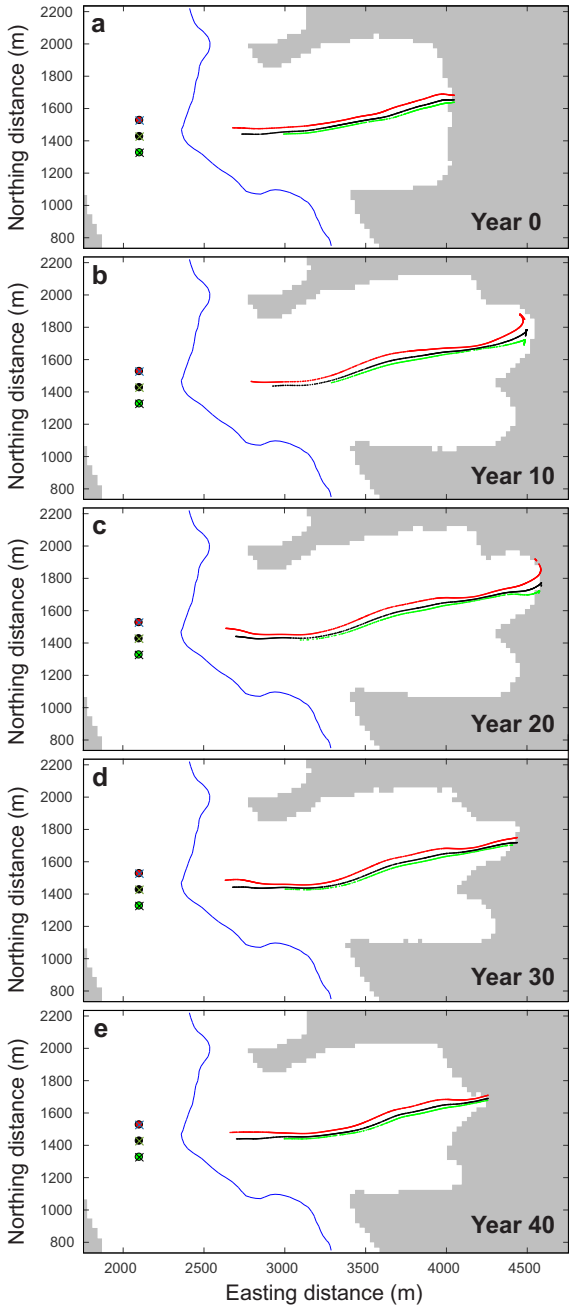


**Figure 15.** Simulated medial moraines for Trapridge Glacier model at various times in the 50-year surge cycle. $N$ denotes any integer. (a) Year 0 (1985±50N). (b) Year 10 (1995±50N). (c) Year 20 (2005±50N). (d) Year 30 (1965±50N). (e) Year 40 (1975±50N). Locations of the debris input point for each of the three moraine stripes (red, black, and green) are indicated by corresponding markers in the glacier accumulation area.

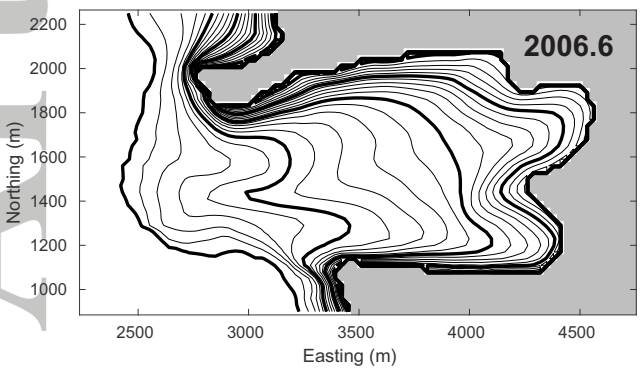


**Figure 16.** Map of simulated $S_0$ stratification for Trapridge Glacier model. The stratification is assumed to be associated with depositional layering so that each deposition surface is isochronal. The contour interval is 10 years. Working from the top-down, thick contour lines correspond to 2000, 1950, 1900, 1850, and 1800. The observation year is 2006.6 (year 21.6 of the modeled 50-year surge cycle).

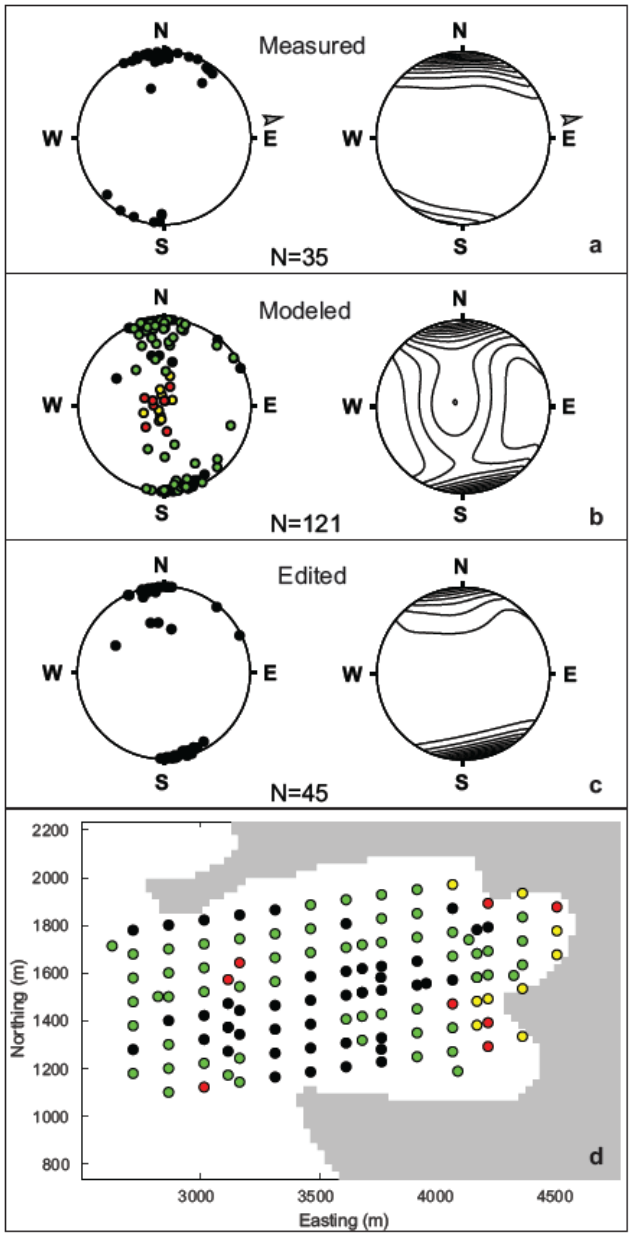


**Figure 17.** Comparison of measured and modeled stereographic projections of the $S_1$ data. (a) Measured. (b) Modeled. (c) Model using edited data to eliminate points that are unlikely to favor development of the $S_1$ foliation. The modeled points are color coded as follows: yellow fill indicates points associated with a low-angle foliation plane (less than 30° dip), green if the axis ratio for the strain ellipsoid is unfavorably low ($\kappa_{2:3} < 5$), or red if both failure criteria are experienced. Black points are acceptable from both perspectives. (d) Map of measurements sites for modeled foliation. Black circles indicate the 15 locations where the model predicts $S_1$ foliations would be developed.

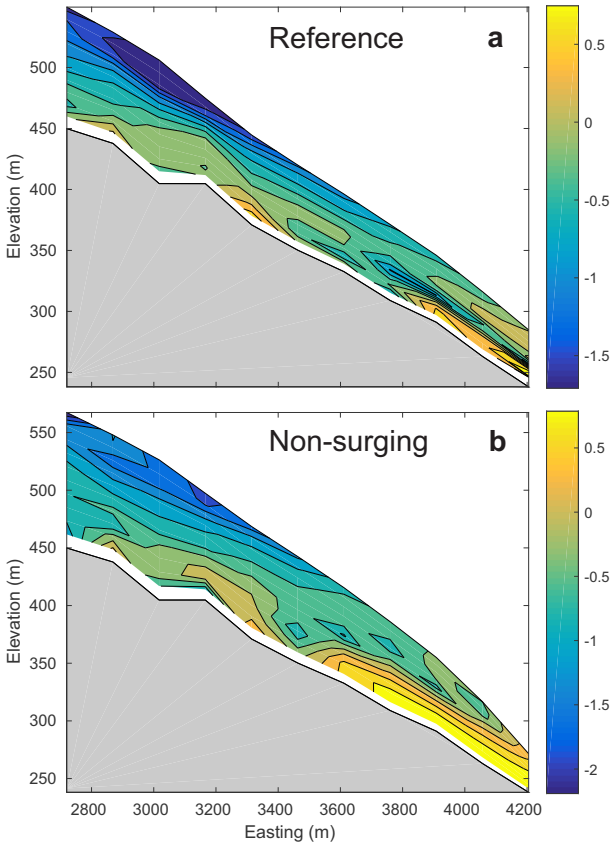


**Figure 18.** Simulated longitudinal profile of folded ice for Trapridge Glacier models. The contoured variable is $\log_{10} \mathcal{Q}_2$ where $\mathcal{Q}_2$ is a fold index. Observation year is 2006.6. (a) Reference model. (b) Non-surging model.

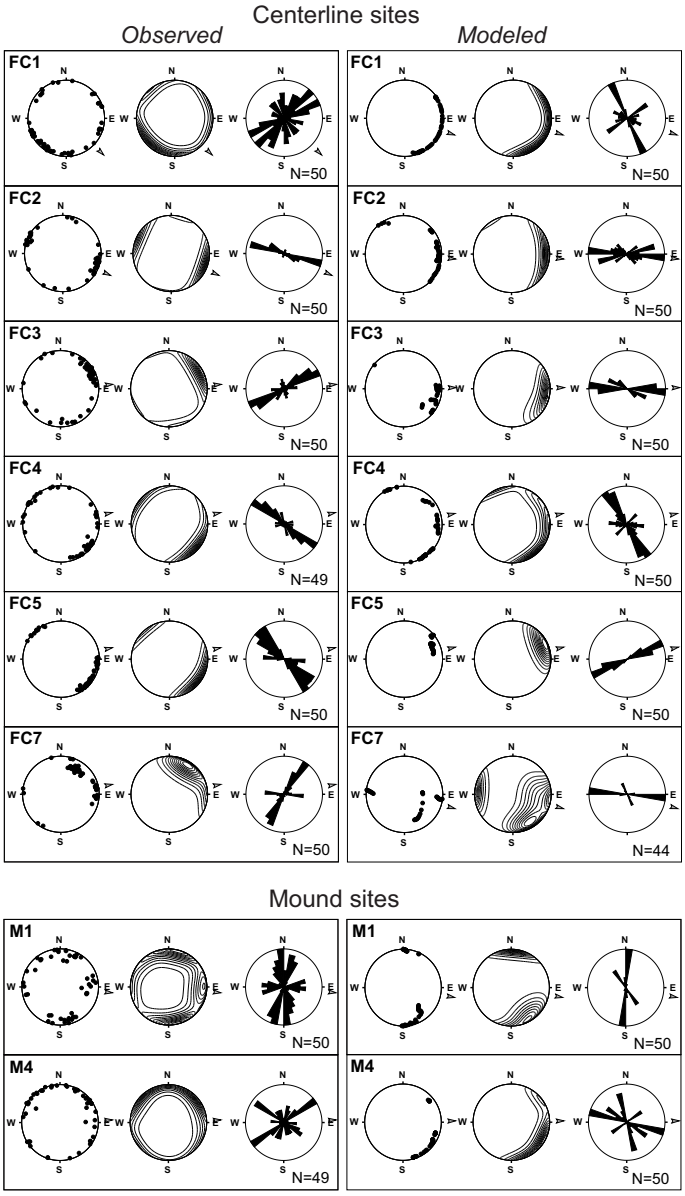


**Figure 19.** Comparison of measured and modeled crevasse trace data at FC and M measurement sites for Trapridge Glacier. Each panel shows simulation results in the form of a Schmidt diagram (equal-area, lower hemisphere projections of poles of crevasse traces), a contoured density plot of the same data, and a rose diagram of the dip directions of the crevasse traces. Arrows (roughly eastward-pointing) indicate the inferred or modeled ice flow direction. Observation year is 2006.6 (year 21.6 of modeled 50-year surge cycle).

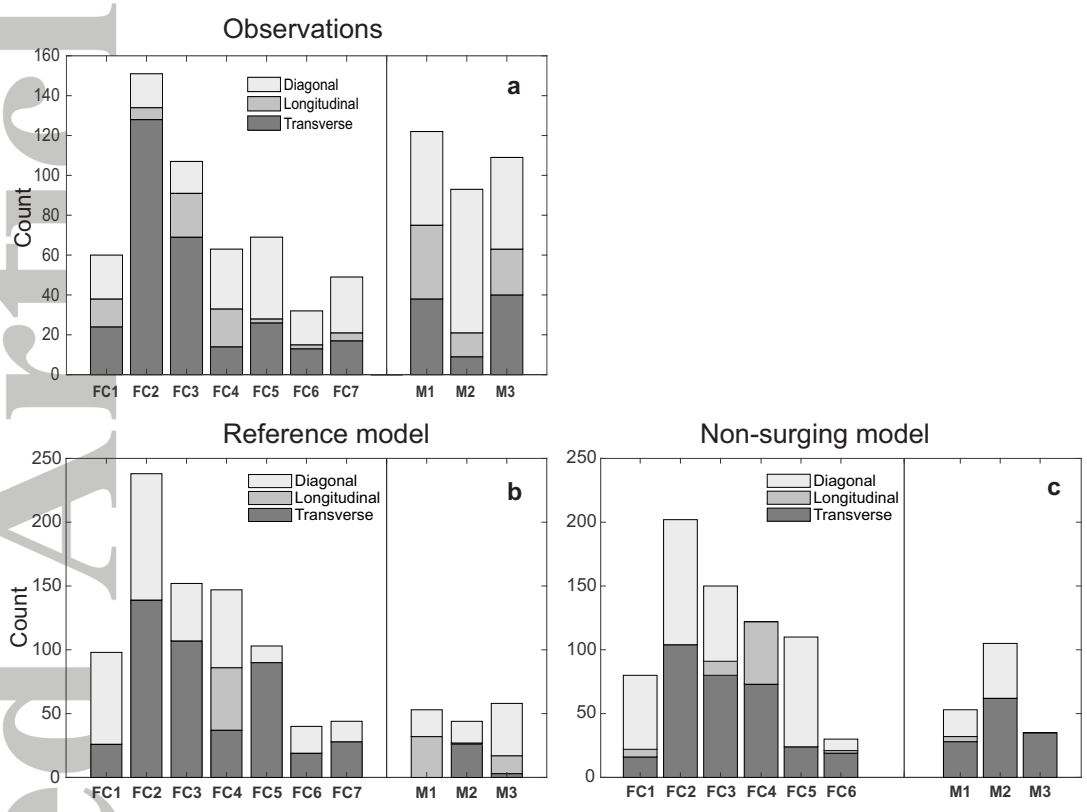


**Figure 20.** Observed and simulated fracture (crevasse trace) counts for flow centerline (FC) and surface mound (M) sites of Trapridge Glacier. Observation year is 2006.6 (year 21.6 of the 50-year surge cycle). (a) Observed. (b) Trapridge reference model. (c) Trapridge non-surging model. For the non-surging model, site FC7 was off-glacier at 2006.6.

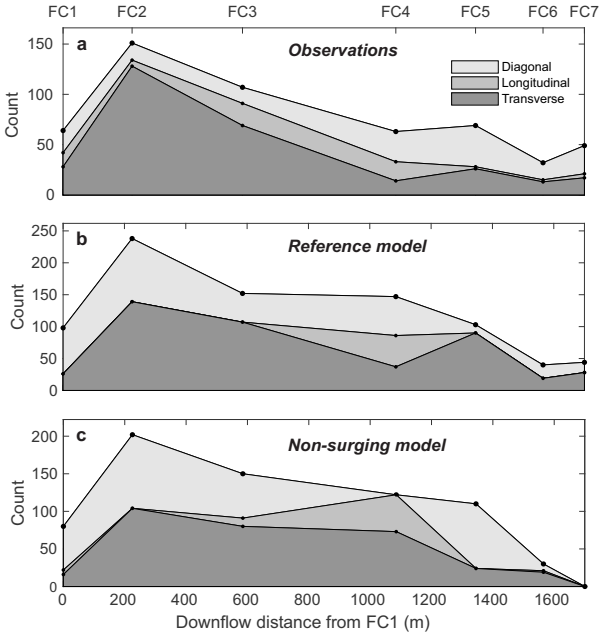


**Figure 21.** Observed and simulated crack counts along flow centerline (FC) of Trapridge Glacier. Observation year is 2006.6 (year 21.6 of the 50-year surge cycle). (a) Observed. (b) Trapridge reference model. (c) Trapridge non-surging model. Note that for the non-surging model site FC7 was off-glacier.

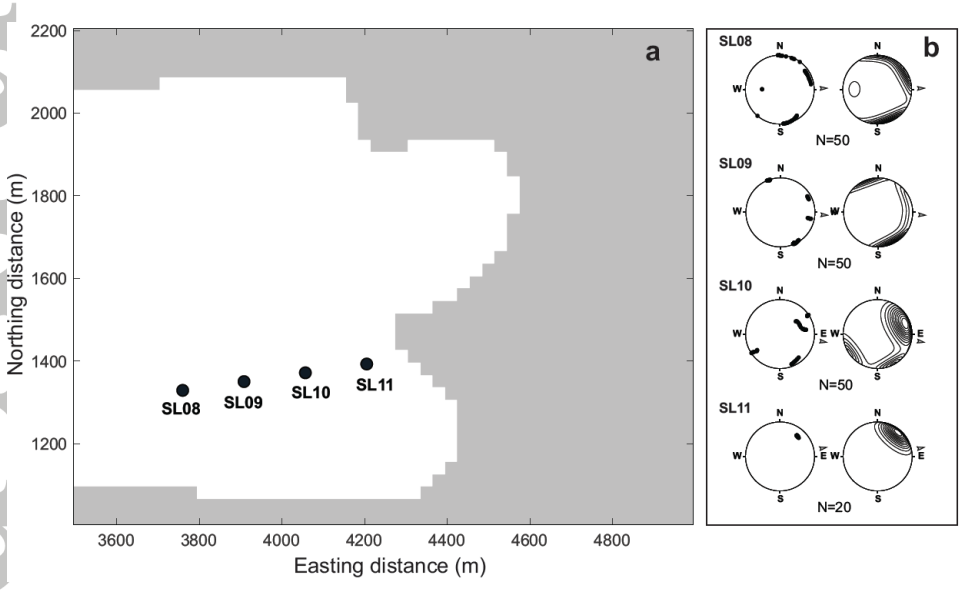


**Figure 22.** Simulated orientation of surface cracks at centerline sites (but not field measurement sites) near the terminus of Trapridge Glacier. Observation year is 2006.6 (year 21.6 of the 50-year surge cycle). (a) Map showing site locations. (b) Schmidt diagrams (equal-area, lower hemisphere projections of poles of crevasse traces) and contoured point density plots for the same simulation results.

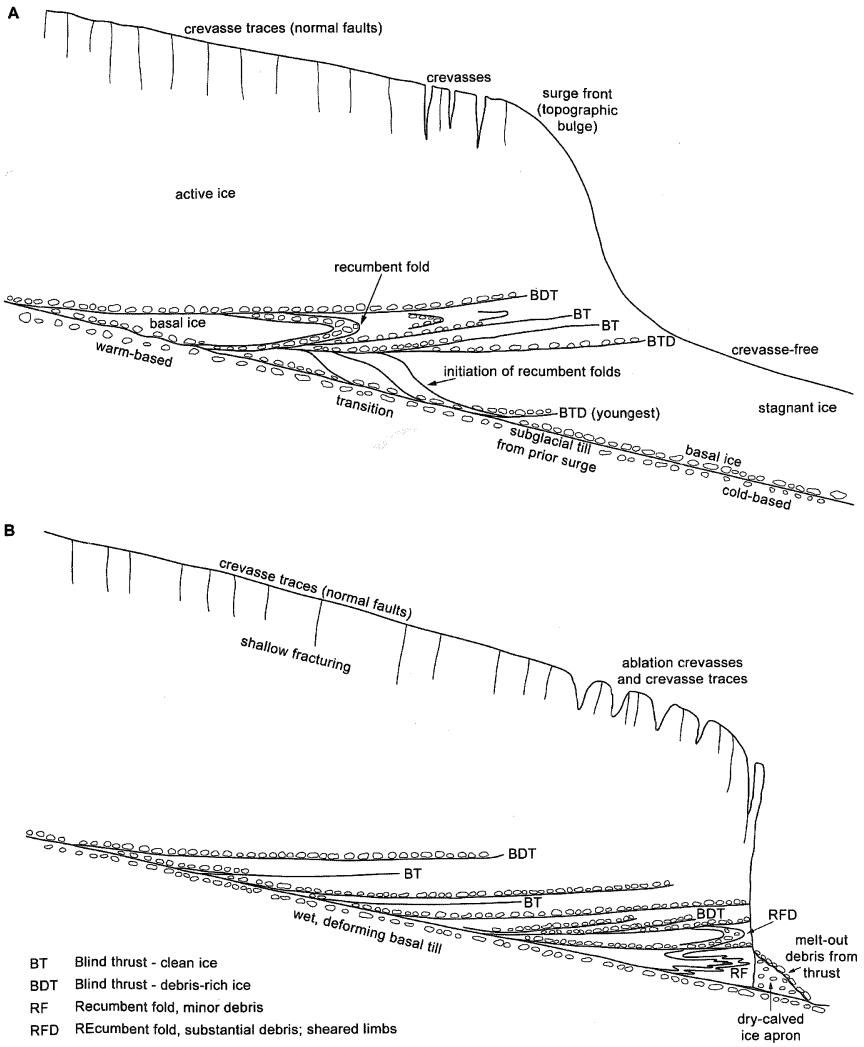


**Figure 23.** Conceptual model of structural evolution, focusing on recumbent folding and thrusting during (a) the slow surge, and (b) surge termination when surge front reaches the snout.